International Journal of Wildland Fire, 2002, **11**, 213–232

An examination of the sensitivity of numerically simulated wildfires to low-level atmospheric stability and moisture, and the consequences for the Haines Index

Mary Ann Jenkins

Department of Earth and Atmospheric Science, Faculty of Pure and Applied Science, York University, 4700 Keele Street, Toronto, Ontario, Canada, M3J 1P3. Telephone: +1 416 736 5245; fax: +1 416 736 5817; email: maj@yorku.ca

This paper is derived from a presentation at the 4th Fire and Forest Meteorology Conference, Reno, NV, USA, held 13–15 November 2001

Abstract. The Haines Index, an operational fire–weather index introduced in 1988 and based on the observed stability and moisture content of the near-surface atmosphere, has been a useful indicator of the potential for high-risk fires in low wind conditions and flat terrain.

The Haines Index is of limited use, however, as a predictor of actual fire behavior. To develop a fire–weather index to predict severe or erratic wildfire behavior, an understanding of how the ambient lower-level atmospheric stability and moisture affects the growth of a wildfire is needed. This study is a first step in this process. This study investigates, through four comparative numerical simulations with a coupled wildfire–atmosphere model, the sensitivity of wildland fires to atmospheric stability and moisture, and in the process explores the correspondence between atmospheric stability and moisture, wildfire behavior, and the Haines Index. In the first three fire simulations, the model atmosphere was initially set to identical moisture but different instability conditions that correspond to Haines Indexes for low, moderate, and high potential for severe fire development. In the fourth fire simulation, the initial atmospheric and moisture conditions were for a high-risk fire Haines Index rating, but different from the initial conditions of dryness and stability of the previous experiments. The study indicates that high-risk fire development is sensitive to near-surface atmospheric stability and moisture, and that there is a range of atmospheric stability and moisture conditions that is important to the development of severe or erratic fire behavior, and that this range is within the atmospheric stability and moisture conditions represented by a Haines Index for high potential for severe fire. The analyses also suggest that there is a substantial latitude of fire behavior for fires rated as this Index, indicating that this Index should be further divided, or refined.

Additional keywords: coupled wildfire and atmospheric numerical modelling.

(1) Introduction

Fire practitioners hope that, in order to predict wildfire behavior, wildfire severity is dependent on a relatively small number of observable parameters defining the environments in which wildfires grow. Two parameters believed to be particularly important in influencing wildfire evolution and structure are lower-level atmospheric stability and moisture content. It is generally accepted that dry, unstable air helps determine whether a wildland fire will become as big in vertical as in horizontal extent. Significant vertical column development increases the probability that the wildfire will become large and/or erratic.

Observational studies (Brotak and Reifsnyder 1977; Haines 1988; Brotak 1993; Werth and Ochoa 1993; Potter 1996; Werth and Werth 1998; Jones and Maxwell 1998; Reges and Alden 1998; García Diez *et al.* 1994, 1999) provide evidence of a relationship between unstable environmental lapse rates, dry air, and large or erratic fire growth. Several of these studies investigated correlations between the level of wildfire risk and the Haines Index (Haines 1988), an operational fire–weather index that rates the potential for large fire growth or extreme fire behavior based on the stability and moisture content of the near-surface atmosphere. The products of these studies are useful for understanding what upper-air

 10.1071/WF02006 1049-8001/02/030213

observations may be preferable for computing the Index, and for determining the frequency of high Index values and seasonal variations of the Index for regions in the United States. It is not possible, however, to isolate the effects of near-surface atmospheric stability and/or humidity on wildfire behavior with this approach.

Using the Clark *et al.* (1996*a*, 1996*b*) coupled wildfire–atmosphere numerical prediction model, Coen and Clark (2000) simulated a fire line propagating over a small ridge in an environment forced by terrain, low-level atmospheric stability, and vertical wind shear. The model fire first moved up the ridge and formed an arrow-shaped fire line. The fire's right flank then weakened and died. The left flank, instead of continuing forward, veered sharply along the ridge line before going over the ridge top and down the other side. The ambient wind field was a hyperbolic tangent profile, westerly ($3\,m\,s^{-1}$) at the surface, decreasing with height to 1 km above the ground, and then constant ($-3\,m\,s^{-1}$) aloft. The model atmosphere was statically stable below 500 m, neutral above. In a preliminary simulation but for neutral atmospheric stability, Coen and Clark's model wildfire simply moved straight up the ridge and propagated steadily down the other side. Environmental stability obviously had an effect, but how the environmental stability was responsible for the fire line's deflection along the ridge, yet not enough to prevent the model wildfire from eventually going over the obstacle, was not understood. Whatever the explanation for the fire line's behavior, Coen and Clark (2000) demonstrated that the evolution of the model fire line depends on the atmospheric stability.

These studies make it clear that it is important to understand exactly what are the effects of ambient atmospheric stability and humidity on wildfire behavior if we are to develop a fire–weather index, like the Haines Index, to predict wildfire behavior. The first step in this process is to determine in a systematic and objective way the relative importance of stability and humidity to wildfire growth. By fixing the initial environmental conditions, and then selectively varying the ambient atmospheric stability and/or moisture, it is possible to use a coupled wildfire–atmosphere numerical prediction model to examine the effects of these observable parameters on the evolution of a wildfire. The purposes of this study are therefore to investigate, through comparative numerical simulations with the Clark *et al.* (1996*a*, 1996*b*) model, the sensitivity of wildland fires to atmospheric stability and moisture, and in the process explore the correspondence between atmospheric stability and moisture, wildfire behavior, and the Haines Index. Coupled wildfire and atmospheric numerical modeling is a fairly recent and major advance in the modeling of wildfires, and the reader unfamiliar with the merits of this approach to studying wildfire behavior is referred to Jenkins *et al.* (2001).

Four different numerical fire experiments are presented. In the first three fire simulations, the model atmosphere is set to identical initial moisture conditions, and the sensitivity of the coupled wildfire–atmosphere model to different initial low-level ambient atmospheric stabilities is analysed. The corresponding Haines Indexes of these three model fires are for low, moderate, and high potential for severe fire development. In the fourth fire simulation, both initial conditions of dryness and stability are different from the previous experiments. The Haines Index for this fire is for high potential for severe fire development, and the sensitivity of the coupled wildfire–atmosphere model to these particular stability and moisture conditions is analysed.

Modification of even one aspect of a simulation, such as a different initial condition, affects all the fields simulated by the numerical model. It can be difficult to present information, both quantitative and qualitative, about any particular field and how it compares from experiment to experiment. It is also difficult to try to distinguish one experimental fire from another when there are many variables involved and each have multiple (space, x, y, z, and time, t) dimensions. For the purposes of this study, it is useful to first summarize statistically how one simulated field contrasts another. Here the Taylor diagram (Taylor 2001) is introduced and used to evaluate how closely the model field variables match each other in terms of their correlation, root-mean-square (RMS) difference, and ratio of their variances. The advantage of the Taylor diagram, compared to simply reporting these statistics for each field variable being examined, is that the information is plotted on a single diagram. Taylor statistics indicate what fields are most sensitive to the different initial atmospheric conditions. Using this information, certain fields are selected for further examination. The important temporal and spatial variations of these fields are then analysed to understand how the different initial conditions affect the evolution of each model wildfire, and the more important results are presented.

The paper is organized as follows. The Haines Indexes used to examine the effect of atmospheric stability and moisture on fire behavior are presented in the following section. The atmospheric model and the forest fire model are discussed in Section (3). The experimental set-up is described in Section (4), where the initial environmental atmosphere for each experiment based on its Haines Index is presented. A description of the Taylor diagram is given in Section (5). The Taylor statistics of each numerical experiment are discussed in Sections (6) and (7). Section (6) gives a detailed account of the Taylor statistics for the simulated field variables selected for examination, and Section (7) gives a synopsis of the results in Section (6). The fields that show sensitivity to changes in experimental initial conditions as measured by the Taylor Diagram are chosen for examination in Section (8), where the spatial and temporal differences between experiments are presented. The paper is concluded in Section (9). Although the study is exploratory (based on four fire simulations), it indicates that, within a range of near-surface atmospheric stability and moisture conditions, atmospheric stability and moisture are indeed crucial to the development of severe fire behavior.

(2) The low-elevation Haines Index

The Haines Index (Haines 1988) is calculated by adding a temperature term a to a moisture term b. For fires at low elevation, values from 1 to 3 are assigned to a based on the temperature lapse between 95 and 85 kPa. For fires at low elevation, values from 1 to 3 are assigned to b based on the difference between the dry bulb and dew point temperatures at 85 kPa. The Haines Index varies from 2 to 6. A Haines Index of 2 indicates moist, stable air, and the potential for large fire growth or extreme fire behavior is very low. A Haines Index of 6 indicates dry, unstable air, and the potential for large fire growth or extreme fire behavior is high. The higher the Haines Index, the more likely that the fire behavior is severe. Severe or extreme fire behavior involves energetic fires with high rates of spread or sudden acceleration of the fire front, the development of pyrocumulus, crowning, large-scale spotting caused by firebrands lofted ahead of the fire by wind, and large whirl formation. Severe fires have higher fire-line intensities (defined as a heat flux or rate of fire line spread times the heat per unit area generated by the available fuel). In the following sections, whenever a fire simulation is described as having severe or erratic behavior, it is exhibiting any one of these features.

Table 1 shows the temperature and moisture limits used to compute four different low-elevation Haines Indexes for the four numerical experiments of this study. In the first three experiments, $B = 15°C$ and the moisture term $b = 3$, indicating dry air. The difference between the three Haines Indexes depends on a, where $a + b = 4$, 5, and 6 designates the potential for large fire growth or extreme fire behavior as low, moderate, and high, respectively. Each experiment is named (left column, Table 1) by a and b, and t and q which specify A (temperature lapse) and B (moisture) values. In the fourth experiment, $a3b3/t08q11$, the Haines Index is 6, but in this case both A and B are lower values that those of experiment $a3b3/t11q15$. The initial atmospheric conditions for experiment $a3b3/t08q11$ are not as dry or unstable as the conditions for experiment $a3b3/t11q15$.

Table 1. Description of the Haines Indexes for each numerical experiment, where B is the difference between the dry bulb and dew point temperatures at 85 kPa, A is the temperature lapse between 95 and 85 kPa, and the Haines Index = $a + b$

Experiment	A (°C)	a	B (°C)	b	Haines Index	Large fire potential
$a1b3/t01q15$	1	1	15	3	4	Low
$a2b3/t06q15$	6	2	15	3	5	Moderate
$a3b3/t11q15$	11	3	15	3	6	High
$a3b3/t08q11$	8	3	11	3	6	High

(3) Model description

For the objectives of this study, the Clark atmospheric numerical model (Clark 1977, 1979; Smolarkiewicz 1983, 1984; Clark and Farley 1984; Clark and Hall 1991, 1995) is coupled with the Canadian Forest Service Fire Behavior Prediction System or FBPS (Hirsch 1996). The Clark model is a three-dimensional, non-hydrostatic, numerical prediction model capable of resolving convective-scale motions. It includes vertically-stretched and terrain-following coordinates, and two-way or multilevel grid nesting. The FBPS model code has very low computational requirements and is able to simulate wildfire in a variety of settings. A description of the coupling of the Clark atmospheric model with a wildfire behavior model is given in Clark *et al.* (1996*a*, 1996*b*). For this study canopy drag was neglected and warm rain physics were used. The heating and moistening by radiation and small scale turbulence are parameterized as described by Clark *et al.* (1996*a*, 1996*b*).

Clark *et al.*'s (1996*a*, 1996*b*) simple ignition tracer parameterization has been replaced. The forest fuel is divided into rectangular grids. To trace ignition in the current model, four tracers, assigned to each model fuel cell, identify burning areas and define the fire front within fuel cells. The coordinates of the ignition tracers are time dependent and allow fires of arbitrary orientation and shape to move through a mesh of fuel grids at fire–spread rates directed by the fire-scale winds. When coupled with the FBPS, the tracers move with the flow normal to the local model fire perimeter at the fire spread-rate formula based on the FBPS. The tracer advecting wind and therefore spread rates are prescribed at the height of 15 m above ground level, which represents the top of the canopy.

(4) The experimental set-up

With the exception of experiment $a3b3/t11q15$, one level of mesh refinement with two-way interactive grid nesting was used in the simulations. An inner domain, 1.2 km × 2.4 km in size, was nested within an outer domain, 6 km × 6 km in size. The horizontal grid intervals were $\Delta x = \Delta y = 150$ m in the outer domain and $\Delta x = \Delta y = 50$ m in the inner domain. The near-surface vertical grid spacings were $\Delta z = 40$ m in the outer domain and $\Delta z = 20$ m in the inner domain. The horizontal fuel grid intervals were $\Delta x_{\text{fuel}} = \Delta x/4$ and $\Delta y_{\text{fuel}} = \Delta y/4$. The time intervals were $\Delta t = 1$ s in the outer domain and $\Delta t = 1/3$ s in the inner domain. Preliminary model runs showed that, for experiment $a3b3/t11q15$, it was necessary to add a third and larger outer domain, 18.9 km × 18.9 km in size, to ensure that the innermost domain was not contaminated by outer boundary disturbances. Horizontal grid intervals were $\Delta x = \Delta y = 450$ m and $\Delta t = 3$ s in the outermost domain. In the following sections, the fire domain is the innermost domain, i.e. the domain of smallest grid and time resolution.

The experiments started with a spot fire of radius three times the hypotenuse of a fuel cell, ≈53 m. Although a smaller grid size (e.g. less than 20 m) would better resolve fire-scale features, particularly fire-scale vorticity dynamics, the computing times at this grid spacing would be impracticable for this first study. The 50 m grid size in the fire domain allowed simulations of significant duration to track the evolution of the model fire and yet was able to resolve important larger-scale features associated with fire behavior.

The intent is to examine the differences in wildfire behavior based solely on different initial environmental near-surface atmospheric stabilities and moisture content, and each wildfire having different Haines Indexes. Although variations in terrain and fuel, along with large-scale and local meteorology, are undeniably important to wildfire behavior and characteristics, features considered to be complicating influences that are not necessary to the development and maintenance of severe fire are not included in this initial study. There was no Coriolis force and no topography. The deflection of air by the rotation of the Earth does not impact directly on severe fire behavior. The Haines Index is an indicator of the potential for high-risk fires in low wind conditions and flat terrain, and topography is not a necessary condition for severe fire.

Table 2 shows each of the four experiment's relative humidity (RH, %), initial water vapor mixing ratio (q_v, g kg^{-1}), temperature (T, °C), dew-point temperature (T_d, °C) at the surface pressure P of 100 kPa and pressure levels 95 kPa and 85 kPa. Surface pressure, relative humidity, and temperature were the same for all experiments. Above 85 kPa (approximately 550 m) to a tropopause of 10 km, water vapor decayed exponentially to a minimum of 0.1 g kg^{-1}, and the buoyancy frequency was 0.01 s^{-1}. Above the tropopause to the top of the outer domain (approximately 13 km), the buoyancy frequency was 0.02 s^{-1}. These upper-level environmental conditions are the same as those used by Clark *et al.* (1996*a*, 1996*b*). The model environmental wind was initially set to a constant westerly 3 m s^{-1}.

The model fuel was combustible and plentiful to support a conflagration-type fire, and the initial amount was the same for each experiment. The ground and canopy fuels were homogeneous and equal combinations of Spruce, mature Jack Pine, and immature Jack Pine. The initial mass of the ground fuel was 4 kg m^{-2}, and the initial dry mass of the forest canopy was 1 kg m^{-2}, with a moist/dry ratio of 0.85. The burn rate of the dry ground fuel was 0.04 kg m^{-2} s^{-1} (i.e. ground fuel burned off in 100 s once dry). The burn rate of the dry canopy fuel was 0.033 kg m^{-2} s^{-1} (i.e. canopy fuel burned off in 30 s once dry). The combustion coefficient of 17.0×10^6 J kg^{-1} was applied to each dry fuel type. Three percent of the sensible heat released was used to evaporate the water contained in the ground fuel. It was assumed that approximately 5% of the total energy release is radiative and about half of this, approximately 3%, warms the fuel on the surface. It was assumed that the combustion of cellulose results in a conversion of 56% of the dry fuel's mass to water vapor. In the present formulation, heat flux from the ground fire first goes into drying the canopy. Once the canopy fuel is dry and the ground heat flux exceeds the threshold value of 17.0×10^4 J kg^{-1}, the canopy ignites.

Table 2. Description of the relative humidity *RH*, mixing ratio q_v, temperature *T*, and dew-point temperature T_d at pressure levels 100, 95, and 85 kPa for each experiment

Experiment	Pressure (kPa)	RH (%)	q_v (g kg^{-1})	T (°C)	T_d (°C)
$a1b3/t01q15$	100	50.0	11.76	27.0	16.4
	95	36.8	6.93	22.6	7.7
	85	36.8	7.29	21.6	6.8
$a2b3/t06q15$	100	50.0	11.76	27.0	16.4
	95	36.8	6.93	22.6	7.7
	85	35.6	5.09	16.6	1.7
$a3b3/t11q15$	100	50.0	11.76	27.0	16.4
	95	36.8	6.93	22.6	7.7
	85	33.4	3.42	11.6	−3.3
$a3b3/t08q11$	100	50.0	11.76	27.0	16.4
	95	48.1	9.07	22.6	11.7
	85	46.7	5.85	14.6	3.7

Fuel moisture was deliberately not allowed to respond to changes in surface relative humidity due to the fire and remained constant throughout the simulations. This purposely eliminated any sensitivity of fire combustion and subsequent fire development to changes in fuel moisture. The goal was to examine model fire behavior forced exclusively by the effects of near-surface temperature lapse rate and humidity on the atmosphere, not changing fuel moisture.

The upper-air and surface fields chosen for examination are: u, the x or east–west wind component; v, the y or north–south wind component, w, the z or vertical wind component; B, the buoyancy (as in Clark *et al.* 1996*a*, 1996*b*); Q, the water vapor mixing ratio (same as q_v in Table 2); V_x, the x vorticity component; V_y, the y vorticity component; and V_z, the z vorticity component; The three-dimensional vorticity field is defined as

$$(V_x,\ V_y,\ V_z) = \nabla \times \vec{\mathcal{U}}, \qquad (1)$$

the *curl* of the three-dimensional velocity field $\vec{\mathcal{U}}$.

The surface-only fields chosen for examination are: *CI*, *CL*, *CS*, the intensity, latent heating rate, and sensible heating rate, from the canopy burn; *GI*, *GL*, *GS*, the intensity, latent heating rate, and sensible heating rate, from the ground fuel burn; *SR*, the fire spread rate (as in Hirsch 1996); *TK*, the total kinetic energy; and *PK*, the total perturbation kinetic energy.

The kinetic energy that results from model equations is

$$KE = \frac{1}{2}\left(\overline{\overline{m}^x u^2}^x + \overline{\overline{m}^y v^2}^y + \overline{\overline{m}^z w^2}^z\right), \qquad (2)$$

where m is mass of air per grid volume, and the overbars represent grid averages in the x, y, and z directions. The perturbation kinetic energy is

$$PKE = \frac{1}{2}\left(\overline{\overline{m}^x u'^2}^x + \overline{\overline{m}^y v'^2}^y + \overline{\overline{m}^z w'^2}^z\right), \quad (3)$$

where the primed quantities are deviations from the background or environmental mean. Fields *TK* and *PK* are the sum totals of *KE* and *PKE*, respectively, at each grid volume within the fire domain.

Each experiment was a 2 h simulation, and model field data were output every 4 s. Averages of each field over the burning area and the minimum and maximum field values within the fire domain were determined, and the averages of each field provided N discrete points in time. Averages over the burning area are meant to indicate what happened just in the fire. Maximum and minimum values are meant to indicate the upper and lower limits of field strength anywhere within the fire domain. Taylor plots (next section) were constructed with these data and are, as discussed in the Introduction, used to evaluate how closely the respective field variables from the four experiments match one other.

(5) The Taylor diagram

To determine how environmental atmospheric stability and moisture affects model behavior, Taylor's diagram (Taylor 2001) is used to summarize the overall correspondence between the results from one wildfire simulation and another.

The statistic most often used to quantify pattern similarity is the correlation coefficient R, defined by

$$R = \frac{1/N\sum_{n=1}^{N}(f_n - \bar{f})(r_n - \bar{r})}{\sigma_f \sigma_r}, \quad (4)$$

where f_n and r_n are two variables or fields at N discrete points in time and/or space. The overline denotes a mean value, and σ_f and σ_r are the standard deviations of f and r, respectively. The statistic used to quantify differences in two fields f and r is the RMS difference E, which is defined as

$$E = \left[\frac{1}{N}\sum_{n=1}^{N}(f_n - r_n)^2\right]^{1/2}. \quad (5)$$

To isolate the differences in the *patterns* from the differences in the means of the two fields, E is resolved into two components. The overall 'bias' is defined as

$$\bar{E} = \bar{f} - \bar{r}, \quad (6)$$

and the *pattern* RMS difference by

$$E' = \left\{\frac{1}{N}\sum_{n=1}^{N}\left[(f_n - \bar{f}) - (r_n - \bar{r})\right]^2\right\}^{1/2}. \quad (7)$$

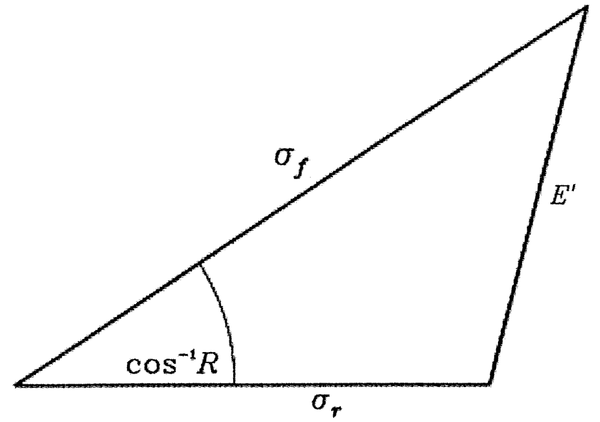

Fig. 1. Geometric relationship between the correlation coefficient R, the pattern RMS difference E', and the standard deviations σ_f and σ_r of the test and reference fields, respectively.

The two components add quadratically to yield the full mean-square difference:

$$E^2 = \bar{E}^2 + E'^2. \quad (8)$$

It is impossible to determine from equation (8) how much difference is due to a difference in phase and how much is due to a difference in the amplitude of the variations for any given value of E'. However, by substituting for R, equation (8) can be rewritten as

$$E'^2 = \sigma_f^2 + \sigma_r^2 - 2\sigma_f\sigma_r R, \quad (9)$$

which is recognized as the Law of Cosines, where σ_f and σ_r and E' are the lengths of the sides of a triangle, and R is the $\cos\phi$ where ϕ ($=\cos^{-1} R$) is the angle opposite the side E'. Equation (9) represents the simple geometrical relationship between four statistical quantities: the correlation coefficient R, the pattern RMS difference E', and the standard deviations σ_f and σ_r. This is illustrated in Fig. 1. Using equation (9), Taylor (2001) constructed a two-dimensional plot that statistically quantifies the degree of similarity between fields f and r, where the four statistical quantities are indicated by a single point. The radial distance from the plot's origin is proportional to the standard deviation of a pattern. The pattern RMS difference between f, the 'test' field, and r, the 'reference' field, is proportional to their distance apart (in the same units as the standard deviation). The correlation between the two fields is given by the azimuthal position of the f field. On a Taylor diagram, the correlation coefficient indicates how much difference is due to phase, and the standard deviations indicate the difference in the amplitude of the variations from the mean for r and f.

(6) The results based on the Taylor diagram

A comparison between three experiments is made in each Taylor diagram. Two of the experiments are chosen as test experiments and one as the reference experiment. Two points connected by an arrow are plotted for each field selected for analysis (Section 4). The tail of the arrow indicates the statistics for the first test experiment, the head of the arrow indicates the statistics for the second test experiment. Because the units of measure are different for each field, their statistics are non-dimensionalized before appearing on the same graph. For each variable, the pattern RMS difference and the standard deviation are normalized by the standard deviation of the corresponding reference field (i.e. $\widehat{E}' = E'/\sigma_r, \widehat{\sigma}_f = \sigma_f/\sigma_r, \widehat{\sigma}_r = 1$). The correlation coefficient is unchanged, and the final statistics yield a normalized Taylor diagram. The standard deviation of the reference field is normalized by itself, and is plotted a unit distance from the origin along the abscissa. For our purposes, experiment $a1b3/t01q15$ is the reference experiment, and experiments $a2b3/t06q15$, $a3b3/t08q11$, and $a3b3/t11q15$ are the tests. The pattern RMS difference and standard deviations are normalized by the standard deviation of each field from model fire $a1b3/t01q15$ before plotting. From this point on, all references to RMS are to *normalized* pattern RMS differences, and all references to standard deviations are to *normalized* variances or standard deviations.

Only a small fraction of the model output can be considered. In this study surface and near-surface model data were used to construct the Taylor diagrams. These are the levels of the atmosphere that fire fighters experience. The model data were sampled at constant time intervals and at a single height level, either at the surface, or at 15 m above ground level, the top of the canopy. The statistics required by equation (9) were computed and plotted on the Taylor diagram. Since the statistics in equation (9) vary according to the sampling frequency, Taylor diagrams based on different constant time intervals (i.e. 5 s, 2 min, and 5 min) were produced and compared. There were differences in the diagrams, but overall trends were consistent, and a sampling frequency of 5 s was used to prepare the final Taylor diagrams. Although each experiment was simulated for 2 h, there was significant variation in the evolution of each fire within the first hour of simulation, and output from this time period was therefore used to produce the Taylor statistics and plots.

The Taylor statistics for model fire $a1b3/t01q15$, designated as having a low potential for severe fire growth, and model fire $a2b3/t06q15$, designated as having a moderate potential for severe fire growth, are given in the following Figs 2–5 and Fig. 10. The statistical differences indicate the relative importance of increased initial atmospheric instability on wildfire growth when the low-level atmospheric is dry. The Taylor statistics for model fire $a3b3/t08q11$, designated as having a high potential for severe fire growth, are also given. In this case, the statistics indicate the relative importance of further decreased initial atmospheric stability, but slightly increased initial humidity, on wildfire growth.

The Taylor statistics comparing model fires $a1b3/t01q15$ and $a2b3/t06q15$ with model fire $a3b3/t11q15$, designated as having a high potential for severe fire growth, are given in the following Figs 6–10. The statistical differences indicate the relative importance of decreasing initial atmospheric stability on wildfire growth for the same initial low-level humidity.

(a) Experiments a2b3/t06q15 and a3b3/t08q11 compared to a1b3/t01q15

Figure 2 shows the Taylor statistics based on averages over the burning area for reference experiment $a1b3/t01q15$ and test experiment $a2b3/t06q15$ (tails of arrows). Except for u, v, and V_x, fields from experiment $a2b3/t06q15$ lie relatively close to the reference point. The RMS differences are relatively small (less than or equal to 0.5), and the correlation coefficients between these fields and the reference field are relatively large (approximately greater than 0.9). The standard deviations of fields B, Q, and V_y are near 1.0, and the standard deviations of fields w and V_z show an overall *reduction* in the amplitude of the variations compared to that of the reference ($\widehat{\sigma}_f < 1$). Field Q has the same amplitude of variations compared to the reference ($\widehat{\sigma}_f \approx 1$), and are nearly completely in phase ($R > 0.99$).

Figure 2 shows the fields from experiment $a2b3/t06q15$ (tails of arrows) that have changed most compared to the reference are u, v, and V_x. The RMS difference of 1.07 for u is due primarily to the poor correlation ($R \approx 0.35$) and not the difference in the amplitude of variations ($\widehat{\sigma}_f \approx 0.9$). The RMS difference of 3.06 for V_x is due to a poor and negative correlation ($R \approx -0.4$) combined with a moderate difference in the amplitude of variations ($\widehat{\sigma}_f \approx 2.5$). The RMS difference of 3.4 for v is due to a negative correlation ($R \approx -0.9$) and a moderate difference in the amplitude of the variations ($\widehat{\sigma}_f \approx 2.5$).

Figure 2 also shows the Taylor statistics of experiment $a3b3/t08q11$ (heads of arrows) compared to the reference experiment. Except for u, v, and V_x, the RMS differences for experiment $a3b3/t08q11$ are greater than the RMS differences for experiment $a2b3/t06q15$ (the heads of the arrows lie further away from the reference point than the tails). The arrows are oriented such that the variances are *smaller* in experiment $a3b3/t08q11$ compared to experiment $a2b3/t06q15$ (tails of arrows), and the correlations between experiment $a3b3/t08q11$ (rated as having a high potential for severe fire behavior) and the reference are even further reduced compared to those of experiment $a2b3/t06q15$ (rated as having a moderate potential for severe fire behavior) and the reference for fields w, B, Q, and V_y. For these fields, $\widehat{E}'$ is greater than 0.6 and less than or equal to 0.9, R is approximately greater than 0.6 and less than 0.8, and $\widehat{\sigma}_f$ ranges from 0.5 for V_z to almost 1.0 for V_y.

Figure 2 shows that the fields from experiment $a3b3/t08q11$ that have changed most significantly compared to experiment $a2b3/t06q15$ and the reference experiment are u, v, and V_x. For these fields, the RMS differences are

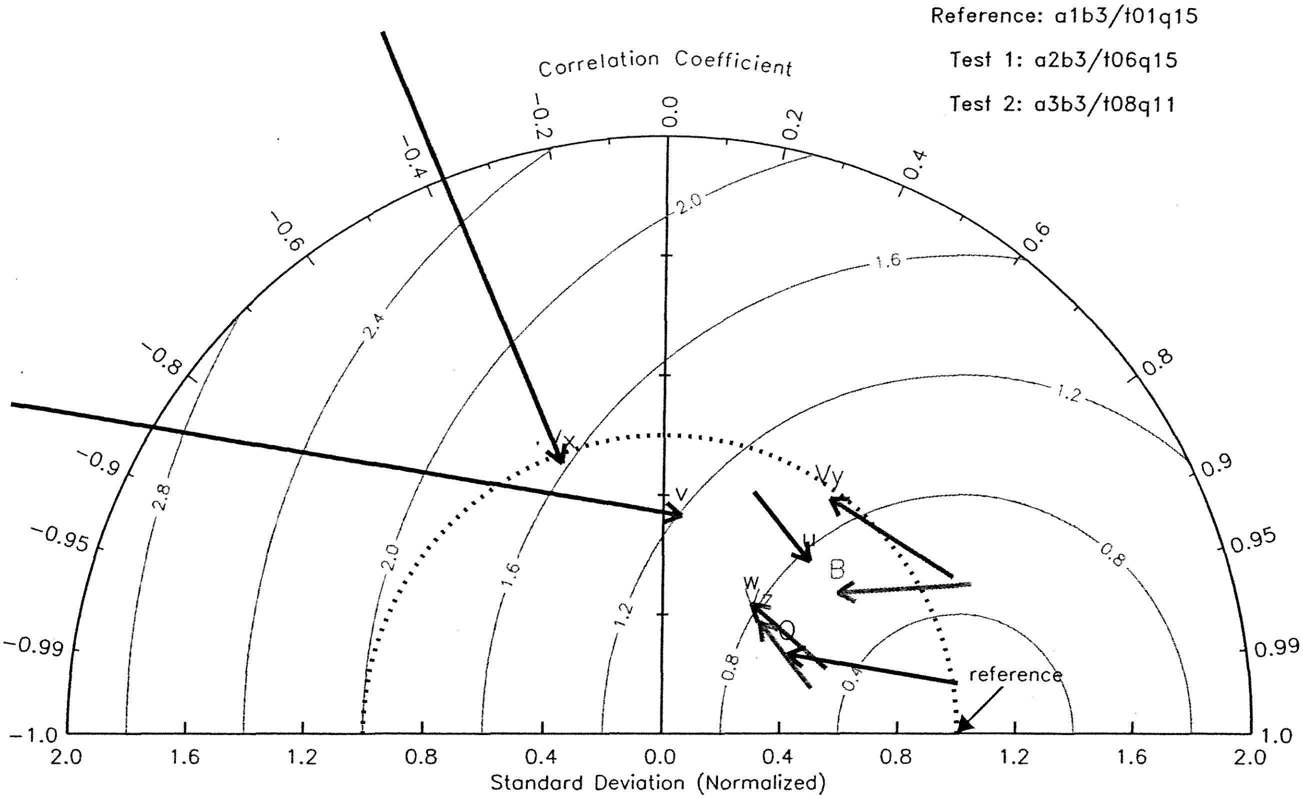

Fig. 2. Changes in normalized pattern statistics between experiments $a2b3/t06q15$ and $a3b3/t08q11$. Statistics for experiment $a2b3/t06q15$ are plotted at the tails of the arrows, and the statistics for experiment $a3b3/t08q11$ are plotted at the heads of the arrows. The pattern RMS difference and standard deviations are normalized by the standard deviation of each field from the reference experiment $a1b3/t01q15$ before plotting. The fields shown are: u, the x or east–west wind component; v, the y or north–south wind component, w, the z or vertical wind component; B, the buoyancy; Q, the q_v water vapor mixing ratio; and V_x, V_y, and V_z, the x, y, and z vorticity components, respectively. For each field, the data were sampled every 5 s between a 4 to 3600 second time period, at 15 m above ground level, and averaged over the burning area. The dotted line represents $\widehat{\sigma}_r$, a unit distance from the origin.

decreased compared to experiment $a2b3/t06q15$ (the heads of the arrows lie closer to the reference point than the tails), the amplitudes of the variations are *reduced* compared those of experiment $a2b3/t06q15$, and the correlations are either nearly zero ($R \approx 0.09$ for v), still positive but reduced ($R \approx 0.7$ for u), or unchanged ($R \approx -0.4$ for V_x).

Figure 3 shows the Taylor statistics based on minimum values within the fire domain for reference experiment $a1b3/t01q15$ and test experiment $a2b3/t06q15$ (tails of arrows). Most fields lie relatively close to the reference point. Except for v and Q, $\widehat{E}'$ is approximately greater than 0.5 and less than 0.8 and, other than v, fields have similar amplitudes of variations compared to the reference ($\widehat{\sigma}_f \approx 1$). Standard deviations range from 0.97 for V_y to 1.3 for v. Except for v, the correlation coefficients R are approximately greater than 0.71 (for V_x) and less than 0.99 (for Q). Field Q has almost the same phase and the same amplitude of variation as the reference. Field v has the largest RMS difference ($\widehat{E}' \approx 1.3$) which is due to phase or pattern differences ($R = 0.4$) and to a low amplitude of variation ($\widehat{\sigma}_f \approx 1.3$).

Figure 3 also shows the Taylor statistics based on minimum values within the fire domain for experiment $a3b3/t08q11$ (heads of arrows) compared to the reference. Except for v, the RMS differences of experiment $a3b3/t08q11$ have increased compared those of experiment $a2b3/t06q15$ (the arrows point away from the reference point), and range from $\widehat{E}' \approx 0.5$ for Q to 1.2 for V_z. Other than field v, the arrows are oriented such that the variances are nearly equal or *smaller* in experiment $a3b3/t08q11$ (rated a Haines Index 6) compared to experiment $a2b3/t06q15$ (rated a Haines Index 5), and the correlations between experiment $a3b3/t08q11$ and the reference are even further reduced compared to those of experiment $a2b3/t06q15$ and the reference.

Figure 4 shows the Taylor statistics based on maximum values within the fire domain for reference experiment $a1b3/t01q15$ and test experiment $a2b3/t06q15$ (tails of arrows). Figure 4 shows that, except for V_y, all fields lie relatively close to the reference point. $\widehat{E}'$ is between 0.15 for B and 1.19 for V_y and, except for V_x, the R is greater than 0.73. The standard deviations for fields other than u, V_y, and

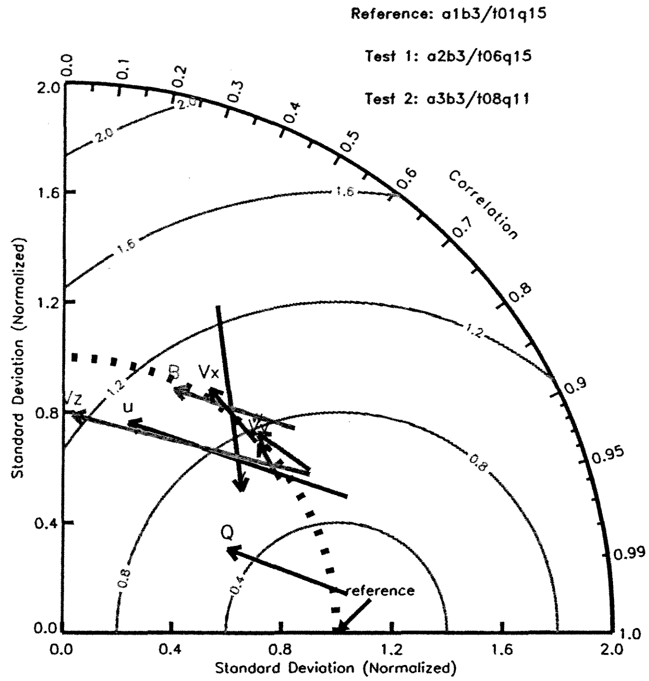

Fig. 3. Same as Fig. 2 except for minimum values in the fire domain.

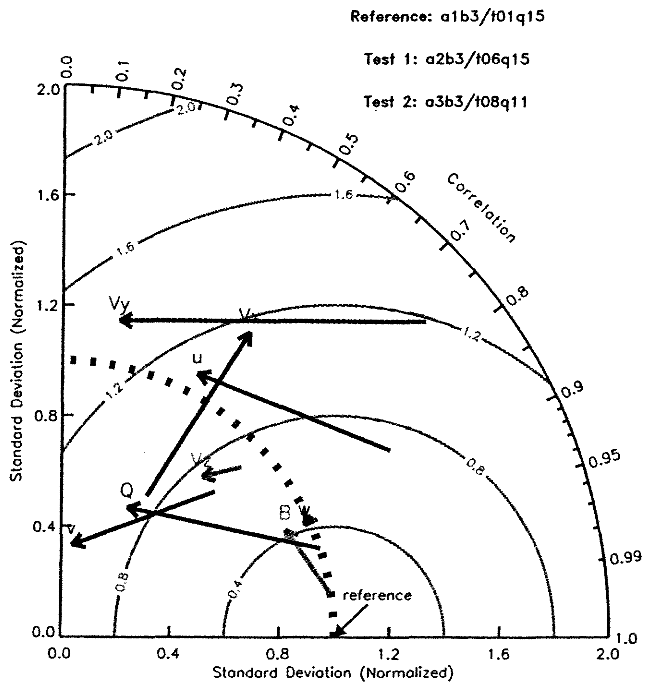

Fig. 4. Same as Fig. 2 except for maximum values in the fire domain.

V_x are close to 1.0, and fields V_z, V_x, and v show an overall *reduction* in the amplitude of the variations compared to that of the reference ($\widehat{\sigma}_f < 1$).

Figure 4 also shows the Taylor statistics based on maximum values within the fire domain for experiment $a3b3/t08q11$ (heads of arrows) compared to the reference. Figure 4 shows that, other than field w, the RMS differences are larger in experiment $a3b3/t08q11$ compared to those in experiment $a2b3/t06q15$ (arrow heads are farther away from the reference point than the tails), and range from $\widehat{E}' \approx 0.4$ for B and w to $\widehat{E}' \approx 1.4$ for V_y. Except for V_x, the arrows are oriented such that the variances in experiment $a3b3/t08q11$ are *smaller* than the variances in experiment $a2b3/t06q15$. The arrows for every field except w and V_x are oriented such that the correlation coefficients in experiment $a3b3/t08q11$ are *reduced* compared to the correlation coefficients for experiment $a2b3/t06q15$. The least significant change is in w (the smallest arrow), and the most significant change is in V_y (the largest arrow). The Taylor statistics for w (where w data were sampled close to the surface) remain essentially unchanged.

The Taylor statistics based on averages of surface-only variables over the burning area experiments $a2b3/t06q15$ (tails of arrows) and $a3b3/t08q11$ (heads of arrows) are given in Fig. 5. Figure 5 shows that fields *CI*, *CL*, *CS*, *GL*, and *GS* from experiments $a2b3/t06q15$ and $a3b3/t08q11$ have the same amplitude of variations compared to the reference ($\widehat{\sigma}_f \approx 1$) and are nearly in phase ($R \approx 1$). The fields that have changed somewhat compared to the reference are *GI* and *SR*. *SR* is the longest arrow in the plot ($\widehat{E}'$ changed from 0.3 in experiment $a2b3/t06q15$ to 0.5 in experiment $a3b3/t08q11$), and the arrow is oriented such that the correlation coefficient and variance in amplitude are *smaller* in experiment $a3b3/t08q11$ ($R \approx 0.89$, $\widehat{\sigma}_f \approx 0.9$) compared to experiment $a2b3/t06q15$ ($R \approx 0.96$, $\widehat{\sigma}_f \approx 1.1$). Comparable RMS differences for *GI* have increased only slightly.

The Taylor statistics based on maximums of the same variables as in Fig. 5 and for test experiments $a2b3/t06q15$ and $a3b3/t08q11$ were also plotted but are not shown. The RMS differences in experiment $a3b3/t08q11$ are larger than the RMS differences in experiment $a2b3/t06q15$ for all fields plotted, and range from approximately 0.06 for *CI* to 0.8 for *SR*. All arrows are oriented such that there is very little difference in the variance in amplitude for experiments $a3b3/t08q11$ and $a2b3/t06q15$ compared to the reference, and that the correlations of experiment $a3b3/t08q11$ with the reference are reduced compared to those of experiment $a2b3/t06q15$. The RMS differences, standard deviations, and correlation coefficients for fields *GL*, *GS*, and *CI* are very similar for experiments $a2b3/t06q15$ and $a3b3/t08q11$. And as in Fig. 5, the fields from experiments $a2b3/t06q15$ and $a3b3/t08q11$ that have changed somewhat compared to the reference are *GI* and *SR*.

The Taylor statistics for fields *TK* and *PK* for test experiments $a2b3/t06q15$ (tails of arrows) and $a3b3/t08q11$ (heads of arrows) are shown in Fig. 10 (upper plot). The RMS differences of experiment $a3b3/t08q11$ are larger compared to experiment $a2b3/t06q15$ (long arrow lengths and the heads of arrows lie further away from the reference point

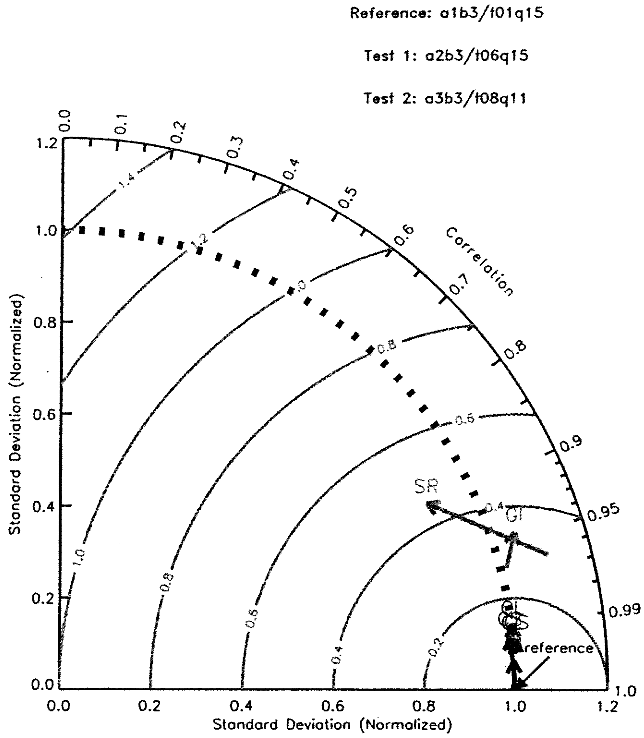

Fig. 5. Changes in normalized pattern statistics between experiments $a2b3/t06q15$ and $a3b3/t08q11$. Statistics for experiment $a2b3/t06q15$ are plotted at the tails of the arrows, and the statistics for experiment $a3b3/t08q11$ are plotted at the heads of the arrows. The pattern RMS difference and standard deviations are normalized by the standard deviation of each field from the reference experiment $a1b3/t01q15$ before plotting. The fields shown are: *CI*, *CL*, *CS*, the intensity, latent heating rate, sensible heating rate, from the canopy burn; *GI*, *GL*, *GS*, the intensity, latent heating rate, sensible heating rate, from the surface fuel burn; and *SR*, the fire spread rate; For each field, the data were sampled every 5 s between a 4 to 3600 second time period, at 0 m above ground level and averaged over the burning area. The dotted line represents $\widehat{\sigma}_r$, a unit distance from the origin.

than tails). The arrow for *TK* is oriented such that the variance in amplitude for experiment $a3b3/t08q11$ is *decreased* compared to $a2b3/t06q15$ ($\widehat{\sigma}_f$ dropped to 1.4 from 1.9), the correlation is significantly reduced (R dropped to -0.07 from 0.89), and the RMS differences are increased somewhat ($\widehat{E}'$ changed to 1.8 from 1.1). Similarly the arrow for *PK* is oriented such that the variance in amplitude for experiment $a3b3/t08q11$ is also *decreased* compared to $a2b3/t06q15$ ($\widehat{\sigma}_f$ dropped to 1.1 from 1.4), the correlation is significantly reduced (R dropped to 0.36 from 0.99), and the RMS difference is increased ($\widehat{E}'$ changed to 1.2 from 0.5).

(b) Experiment a3b3/t11q15 compared to experiments a2b3/t06q15 and a1b3/t01q15

Figure 6 highlights the differences between model fire $a2b3/t06q15$ (tails of arrows), rated a Haines Index 5, and model fire $a3b3/t11q15$ (heads of arrows), rated a Haines Index 6, for Taylor statistics based on the averages over the burning area. The RMS differences of experiment $a3b3/t11q15$ are *substantially* larger compared to experiment $a2b3/t06q15$ (the heads of arrows lie further away from the reference point than tails), with especially dramatic changes in u and v, and then V_y and V_x (very long arrow lengths). $\widehat{E}'$ for experiment $a3b3/t11q15$ ranges from 1.0 for Q to approximately 30 for v. The most dramatic increases occur in u and v, where $\widehat{E}'$ in experiment $a3b3/t11q15$ is changed by a factor of 10 compared to experiment $a2b3/t06q15$. The variances in amplitude in experiment $a3b3/t11q15$ are also increased greatly compared to the variances in amplitude in experiment $a2b3/t06q15$. The standard deviations range from 1.9 for Q to approximately 30 for u and v. Except for Q, the correlation between experiment $a3b3/t11q15$ and the reference is extremely poor ($R < 0.4$). The only field whose Taylor statistics change only moderately is Q (the shortest arrow length). In experiment $a3b3/t11q15$, the Q RMS difference is 1.0, the variance in amplitude is increased, and the correlation coefficient remains nearly 1.0.

Figure 7 shows the Taylor statistics based on the minimums over the burning area for test experiments $a2b3/t06q15$ (tails of arrows) and $a3b3/t11q15$ (heads of arrows). The RMS differences for experiment $a3b3/t11q15$ are greatly increased compared to experiment $a2b3/t06q15$ (arrows point away from the reference point), with fields u and V_y, and then v and B, increasing the most (the longest arrows). The most dramatic increases occur in u and V_y, where the RMS differences in experiment $a3b3/t11q15$ are changed by a factor of 10 compared to experiment $a2b3/t06q15$. The variances in amplitude are also much larger in experiment $a3b3/t11q15$ compared to experiment $a2b3/t06q15$ and the reference experiment $a1b3/t06q15$. For example, $\widehat{\sigma}_f$ for V_y is approximately seven times greater in experiment $a3b3/t11q15$ compared to experiment $a2b3/t06q15$. The correlation between experiment $a3b3/t11q15$ and the reference is poor ($R \approx 0.6$ for w) to extremely poor ($R \approx -0.2$ for B), and fields B and u show negative correlations. $\widehat{E}'$ for experiment $a3b3/t11q15$ ranges from 1.0 for Q to 7.8 for u, and the $\widehat{\sigma}_f$ ranges from 1.7 for Q to 7.7 for V_y and u. The field whose change is most moderate is Q ($\widehat{\sigma}_f \approx 1.7$, $R \approx 0.9$).

Figure 8 shows the Taylor statistics based on the maximums over the burning area for test experiments $a2b3/t06q15$ (tails of arrows) and $a3b3/t11q15$ (heads of arrows). The RMS differences for experiment $a3b3/t11q15$ have dramatically increased compared to experiment $a2b3/t06q15$ (the arrows are long and point away from the reference point), with field V_y having the biggest increase. The variances are substantially larger in experiment $a3b3/t11q15$ compared to those in experiment $a2b3/t06q15$. For experiment $a3b3/t11q15$, the standard deviations $\widehat{\sigma}_f$ range from 1.0 for buoyancy B to 17.0 for V_y and, except for field V_y, $\widehat{\sigma}_f < 4.2$. For every field other than Q, the correlation

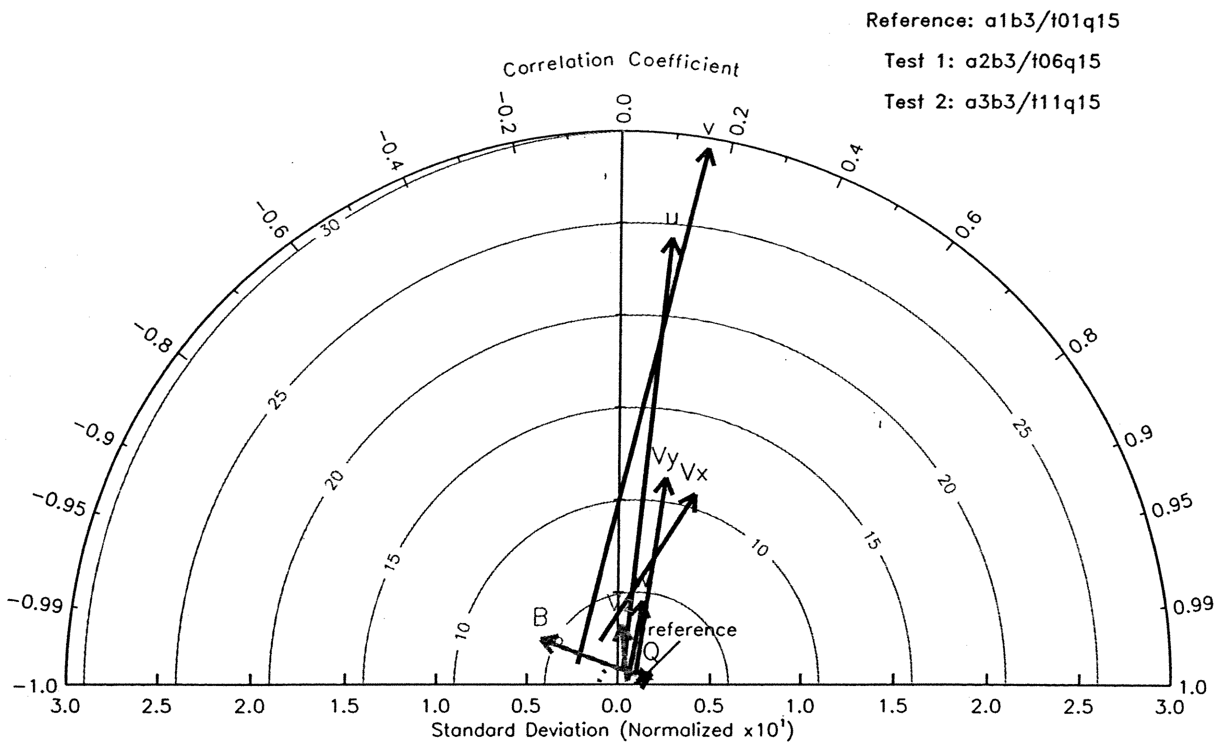

Fig. 6. Changes in normalized pattern statistics between experiments $a3b3/t11q15$ and $a2b3/t06q15$. The statistics for experiment $a2b3/t06q15$ are plotted at the tail of the arrows, and the statistics for experiment $a3b3/t11q15$ at the head of the arrows. The fields shown are the same as those in Fig. 2.

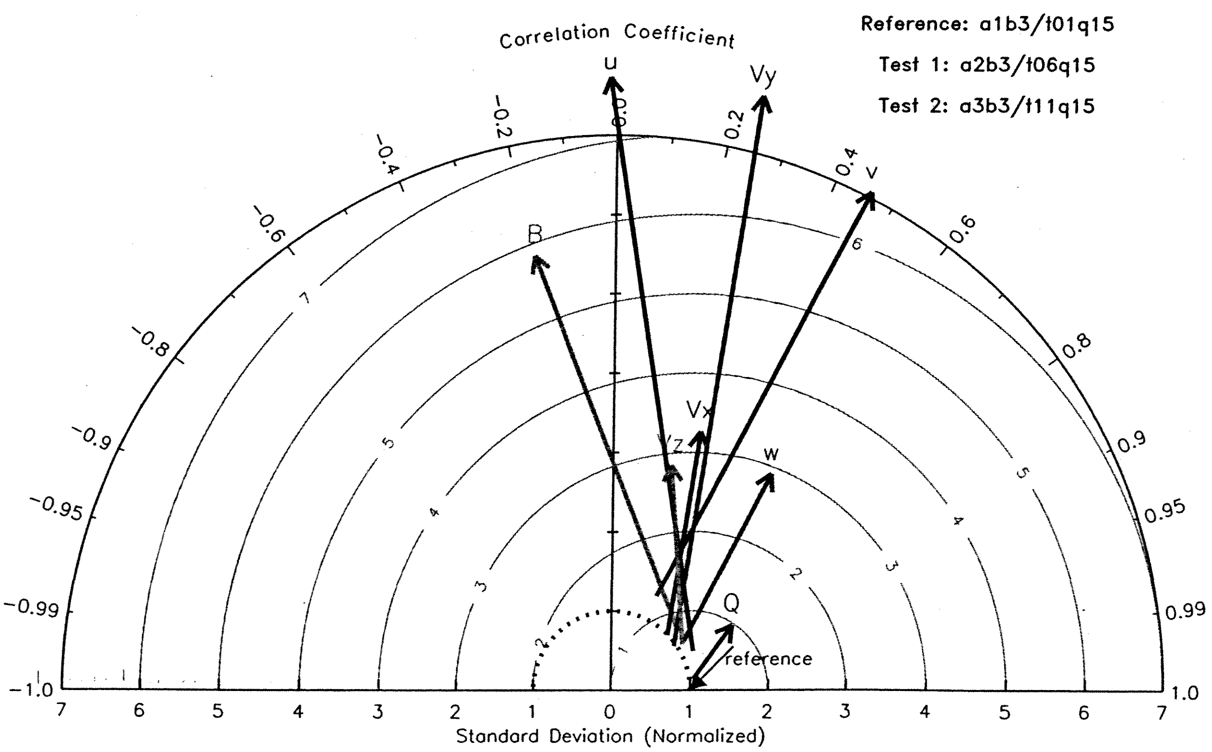

Fig. 7. Same as Fig. 6 except for minimum values in the fire domain.

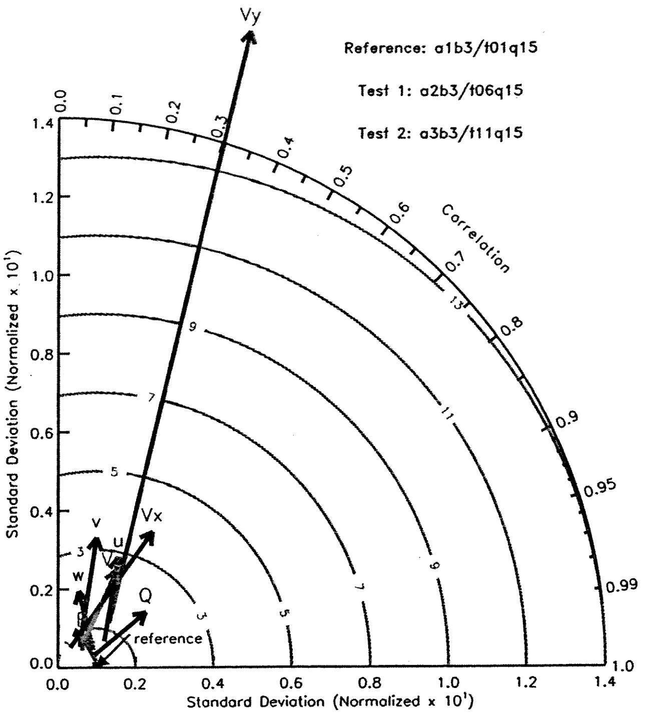

Fig. 8. Same as Fig. 7 except for maximum values in the fire domain.

between experiment $a3b3/t11q15$ and the reference is positive but moderately poor ($R \approx 0.6$ for Q) to poor ($R \approx 0.2$ for v, w, and V_y). The $\widehat{E}'$ is greater than 0.9 for B and less than or equal to 16.7 for V_y and, except for field V_y, $\widehat{E}' < 3.7$. The field whose Taylor statistics change the least in experiment $a3b3/t11q15$ is B (the shortest arrow length); the variance in amplitude is close to 1.0 and the correlation coefficient is 0.6.

The Taylor statistics based on averages of surface-only variables over the burning area for test experiments $a2b3/t06q15$ (tails of arrows) and $a3b3/t11q15$ (heads of arrows) are given in Fig. 9. The RMS differences for experiment $a3b3/t11q15$ are significantly increased compared to experiment $a2b3/t06q15$ (arrows point away from the reference point) for all fields, and the most obvious changes in the Taylor statistics are for fields *CI*, *GI*, and *SR*. The longest arrow is for *CI*, where the $\widehat{E}' \approx 0.03$ (tail of arrow) is increased to 7.3 (head of arrow), $\widehat{\sigma}_f \approx 1.0$ (tail of arrow) is increased to 7.0 (head of arrow), and $R \approx 7.0$ (tail of arrow) drops to 0.1 (head of arrow). The large and simultaneous change in the Taylor statistics for *SR*, *GI*, and *CI* (very long arrows), means that model fire $a3b3/t11q15$ experienced an acceleration in fire-spread rate, accompanied by an increase in heat flux from the ground fuel and then canopy ignition (i.e. crowning).

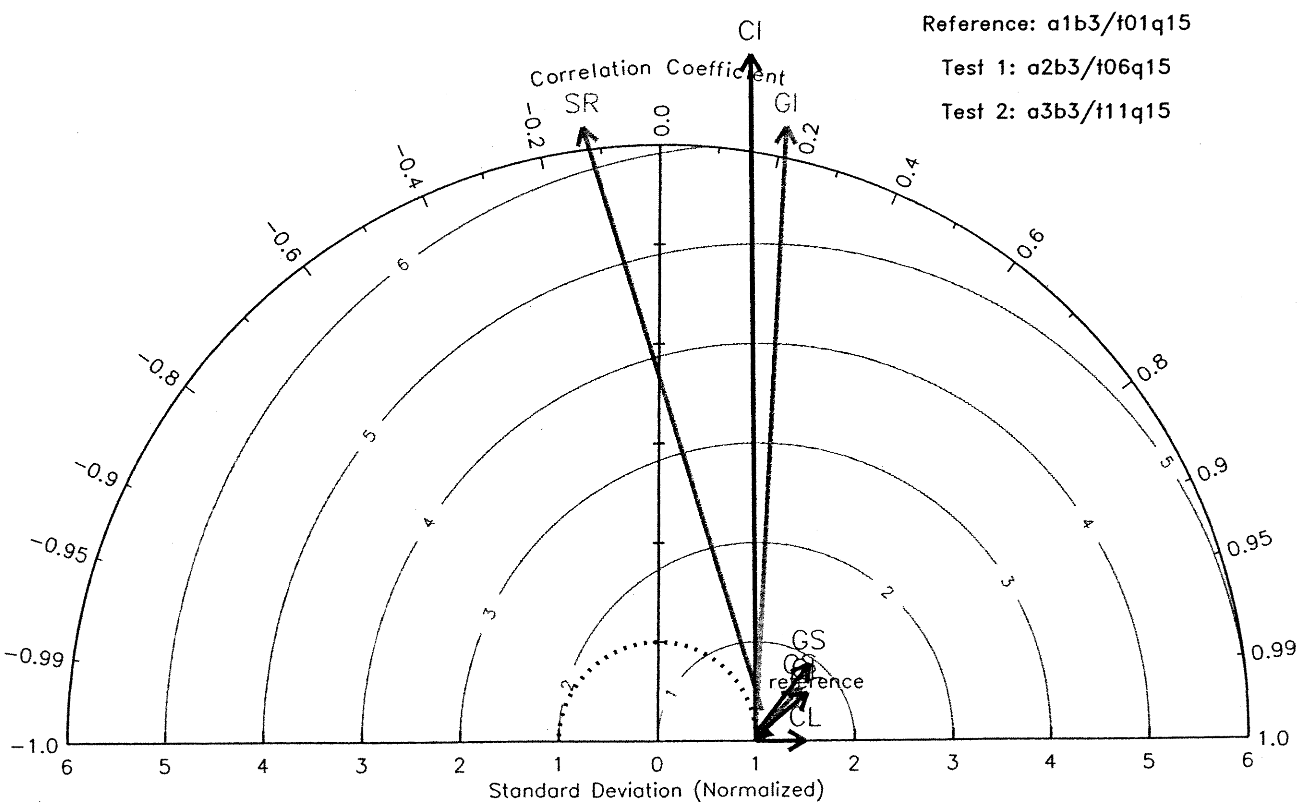

Fig. 9. Same as Fig. 5 except for changes in normalized pattern statistics between experiments $a2b3/t06q15$ and $a3b3/t11q15$. Statistics for experiment $a2b3/t06q15$ are plotted at the tails of the arrows, and the statistics for experiment $a3b3/t11q15$ are plotted at the heads of the arrows.

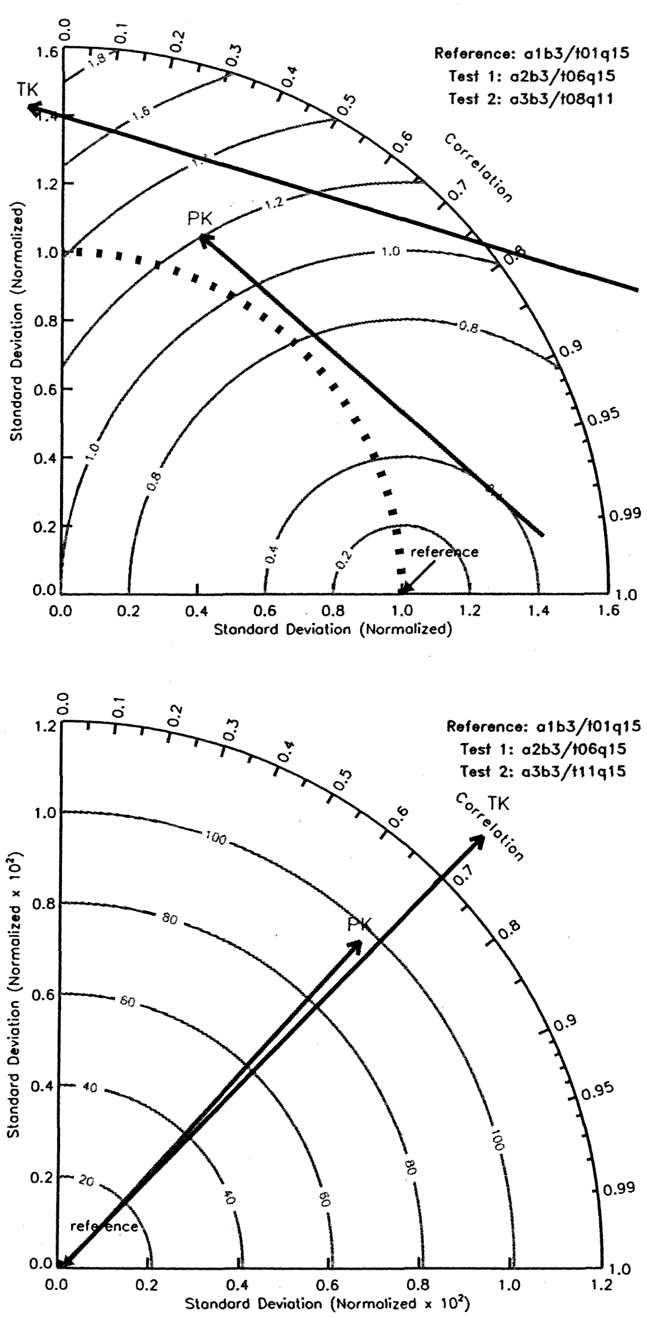

Fig. 10. The upper Taylor diagram shows changes in normalized pattern statistics between experiments $a2b3/t06q15$ and $a3b3/t08q11$. Statistics for experiment $a2b3/t06q15$ are plotted at the tails of the arrows, and the statistics for experiment $a3b3/t08q11$ are plotted at the heads of the arrows. The lower Taylor diagram shows changes in normalized pattern statistics between experiments $a2b3/t06q15$ and $a3b3/t11q15$. Statistics for experiment $a2b3/t06q15$ are plotted at the tails of the arrows, and the statistics for experiment $a3b3/t11q15$ are plotted at the heads of the arrows. The pattern RMS difference and standard deviations are normalized by the standard deviation of each field from the reference experiment $a1b3/t01q15$ before plotting. The fields shown are: *TK*, the total kinetic energy, and *PK*, the perturbation kinetic energy. For each field, the data were sampled every 5 s between a 4 to 3600 second time period, at 0 m above ground level.

The Taylor statistics for the minimum of fire spread rate *SR* in the fire domain for experiments $a2b3/t06q15$ and $a3b3/t11q15$ were also plotted, but are not shown. The arrow for *SR* was oriented such that the variance in amplitude for experiment $a3b3/t11q15$ was significantly increased compared to $a2b3/t06q15$ ($\widehat{\sigma}_f \approx$ increased to 3.4 from 0.94), the correlation dropped to near zero (R changed to 0.16 from 0.95), and the RMS differences increased by a factor of 10 ($\widehat{E}'$ changed to 3.4 from 0.3).

The Taylor statistics for fields *TK* and *PK* for test experiments $a2b3/t06q15$ (tails of arrows) and $a3b3/t11q15$ (heads of arrows) are shown in Fig. 10 (lower plot). The arrows for *TK* and *PK* are oriented such that the RMS difference and variance in amplitude for experiment $a3b3/t11q15$ are dramatically increased (50–100 times greater) compared to $a2b3/t06q15$. Field *TK*, for example, has $\widehat{E}'$ increasing from 1.6 to 52.4, R dropping from 0.9 to 0.7, and $\widehat{\sigma}_f$ increasing from 1.9 to 133.0.

(7) Discussion of Taylor diagram results

The Taylor statistics based on averages over the burning area for experiment $a2b3/t06q15$ show that most fields do not change significantly (i.e. w, B, Q, V_y, and V_z in Fig. 2) when the near-surface atmosphere stays dry and initial atmospheric stability is decreased. Although less than 1, the correlation coefficient for most fields is relatively high, and many fields that might be expected to become more variable with decreased atmospheric stability (i.e. w, u, and V_z in Fig. 2) show an overall *reduction* in the amplitude of the variations (i.e. the tails of the arrows lie within the unit distance from the origin in Fig. 2). For field Q there appear to be no substantive statistical differences between experiment $a1b3/t01q15$, rated as a Haines Index 4, and experiment $a2b3/t06q15$, rated as a Haines Index 5.

The results indicate that a Haines Index 6 does not necessarily mean abrupt changes in fire behavior or growth. The same Taylor statistics for experiment $a3b3/t08q11$ show a *further* overall *reduction* in the amplitude of the variations in most fields (i.e. the heads of the arrows lie closer to the origin than the tails in Fig. 2), while the correlation coefficient for most fields drops. These results suggest the importance of low-level moisture. The Haines Index of 6 for experiment $a3b3/t08q11$ is based on larger initial atmospheric instability, but slightly more humidity. Near-surface humidity may be opposing the effect of larger initial atmospheric instability on the growth of the fire. A few fields do not follow these trends (u, V_x and v) and have moderate statistical differences when initial atmospheric stability is decreased while moisture is increased, as illustrated by the direction, position, or length of arrows.

The trends are slightly different for the Taylor statistics based on the minimum and maximum values within the fire domain for experiments $a2b3/t06q15$ and $a3b3/t08q11$

(Figs 3 and 4). The statistics for experiment $a2b3/t06q15$ show that most fields do change somewhat when the low-level atmospheric stability is decreased, and that most show an expected increase in the amplitude of the variations (i.e. the tails of the arrows lie outside the unit distance from the origin) and drop in correlation. But again, even though experiment $a3b3/t08q11$ has a higher Haines Index rating than experiments $a1b3/t01q15$ and $a2b3/t06q15$, the statistics show overall *reductions* in the amplitude of the variations (i.e. the heads of the arrows lie inside the unit distance from the origin).

The spread rate *SR* and the intensity from the burning gound fuel *GI* are the most statistically varying surface-only fields in experiments $a2b3/t06q15$ and $a3b3/t08q11$, as illustrated by the position and length of arrows in Fig. 5. But these fields show relatively insignificant statistical changes as the Haines Index for experiments $a2b3/t06q15$ and $a3b3/t08q11$ is increased.

The integrated field properties represented by *TK* and *PK* are perhaps best able to compare the Taylor statistics for each experiment. Experiments $a2b3/t06q15$ and $a3b3/t08q11$ have notable statistical differences, as illustrated by the direction, position, and length of arrows in Fig. 10 (upper plot). The Taylor statistics for experiment $a2b3/t06q15$ show that *PK* and *TK increase* in amplitude of the variations (i.e. the tails of the arrows lie outside the unit distance from the origin) when initial atmospheric stability is decreased. Then, despite experiment $a3b3/t08q11$ having a higher Haines Index rating than either experiment $a1b3/t01q15$ or $a2b3/t06q15$, the statistics show a *reduction* in the amplitude of the variations (i.e. the heads of the arrows lie closer to the unit distance from the origin) with a further decrease in initial atmospheric stability and a slight increase in low-level humidity. Correlation coefficients decrease as the Haines Index increases.

The overall impression from Figs 2–5 and Fig. 10 (upper plot) is that, when the model fire is specified by the Haines Index as a low risk (experiment $a1b3/t01q15$) to moderate risk (experiment $a2b3/t06q15$) to low-end high risk (experiment $a3b3/t08q11$) fire, the amplitude of the variations in the model fields are not necessarily increased and the differences in experimental results are due primarily to the larger phase differences or lower correlations between simulated fields. None of these model fires exhibited severe or erratic fire behavior. The Taylor statistics suggest that for fires rated as a Haines Index 5 or lower, the low-level atmospheric stability is important for severe fire risk within the first hour of simulation when humidity is low and the initial ambient conditions include low wind speeds (3 m s^{-1}) with no vertical wind shear, and no topography. For fires rated as Haines Index 6, but at the lower end of the high risk fire rating, the low-level atmospheric stability is not important to severe fire risk within the first hour of simulation if the initial atmospheric moisture is not low enough.

Experiment $a3b3/t11q15$ is rated as a Haines Index 6. The initial near-surface atmosphere was very dry and highly unstable, and the Taylor statistics show that this model fire is very different in strength and severity compared to the previous three. The amplitude of variations increased substantially, in some cases 10-fold or more (i.e. u, v, V_y, in Fig. 6; and V_y in Fig. 8) or even 50–100-fold (i.e. *PK* and *TK* in Fig. 10, lower plot). For the majority of fields the correlation decreased considerably, and in some cases the fields show negative (i.e. *B* in Fig. 6; u in Fig. 7; and *SR* in Fig. 8) or near-zero (u, v, V_y, and V_z in Fig. 6; V_z, V_y, and V_z in Fig. 7; v, w, and V_y in Fig. 8; *CI* and *GI* in Fig. 9) correlation with the reference experiment $a1b3/t01q15$ and experiment $a2b3/t06q15$. The statistics indicate severe fire behavior as described in section (2). There are dramatic and sudden changes in *SR*, *GI*, and *CI*, along with large variations in u, v, and V_y.

The overall impression from Figs 6–9 and Fig. 10 (lower plot) is that, for fires rated as an Haines Index 6, atmospheric stability is the important factor for severe fire risk within the first hour of simulation, provided the near-surface atmosphere is unstable and dry enough. Only this fire experienced severe and erratic fire behavior as high rates of spread and acceleration of the fire front, substantially increased fire intensity from ground and canopy fuel, and crowning.

The statistics also suggest that there is a considerable range of fire behavior for fires rated as a Haines Index 6, and that both low-level humidity and stability are important to the accuracy of this rating. And based on these findings, it is recommended that Index 6 be further divided, or refined.

(8) Dynamic differences between experiments

The Taylor plots in Section (6) indicate that the near-surface fields most sensitive to changes in initial low-level atmospheric stability and moisture are u, v, V_y and *SR*, *GI*, and *CI*. Section (7) concludes that there are major differences between the evolution of fire $a3b3/t11q15$ compared to the evolution of fires $a3b3/t08q11$, $a2b3/t06q15$, and $a1b3/t01q15$. This section therefore describes the important temporal and spatial differences between experiment $a3b3/t11q15$ and experiments $a3b3/t08q11$, $a2b3/t06q15$, and $a1b3/t01q15$. The heat intensities *GI* and *CI* from the burning ground and canopy fuel, the fire spread rate *SR*, and near-surface horizontal winds are presented first.

Figure 11 is a time series plot of average values of *CI*, *GI*, and *SR* over the burning area. The results show that all four model fires behave similarly until approximately 22 min into the simulations. At this time, the fire spread rate *SR* (lower plot) in experiment $a3b3/t11q15$ (dotted line) begins to decrease. At approximately 31 min into the simulation, experiment $a3b3/t11q15$ shows a sudden and dramatic increase in *CI* (upper plot), *GI* (middle plot), and *SR* (lower plot) that lasts 6–7 min. It was with these results that the Taylor plot in

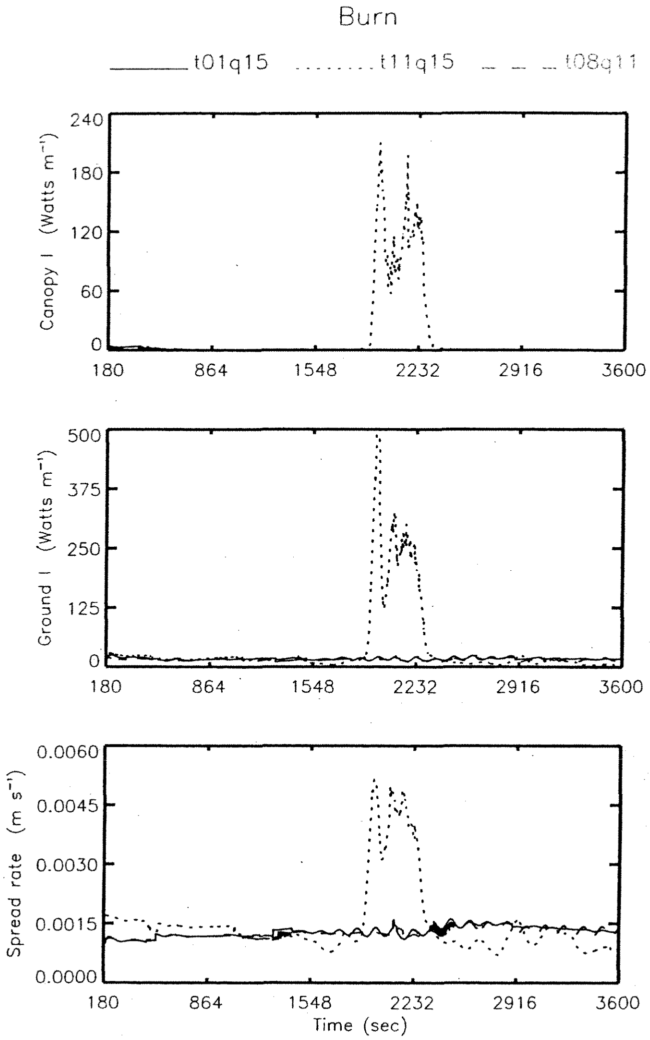

Fig. 11. A time series of average values over the burning area of *CI* (upper plot), *GI* (middle plot), and *SR* (lower plot) for experiments $a1b3/t01q15$ (solid line), $a3b3/t11q15$ (dotted line), and $a3b3/t08q11$ (dashed line).

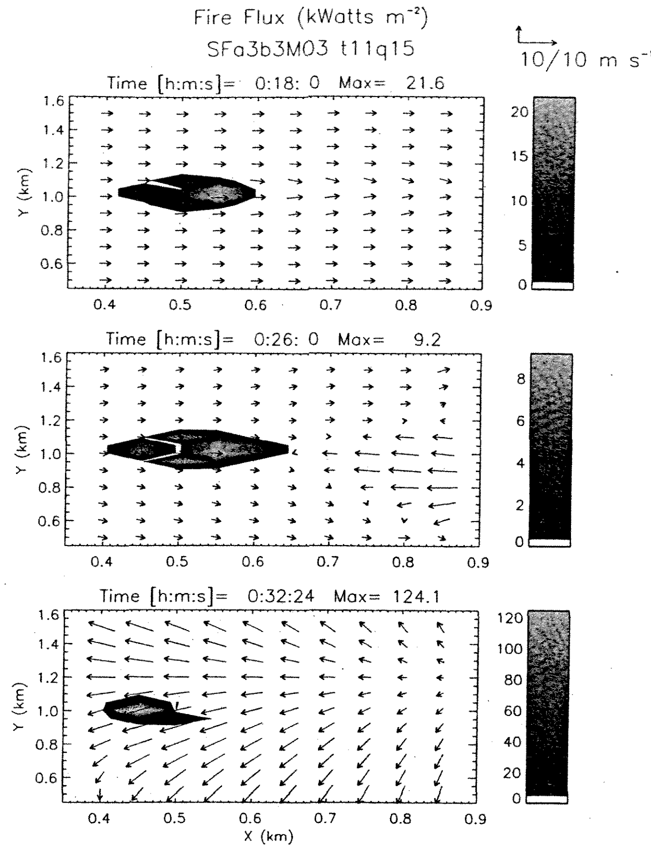

Fig. 12. Fire evolution of the surface fuel ignition for experiment $a3b3/t11q15$. Shaded regions indicate fire fluxes (sensible heat flux in kW m^2). The initial spot fire radius is 53 m. Vectors denote local winds at 15 m above ground level.

Fig. 9 was constructed. For these many minutes, model fire $a3b3/t11q15$ experienced extreme fire behavior: an acceleration in fire-spread rate, accompanied by a dramatic increase in heat flux from the ground fuel, and then canopy ignition (i.e. crowning).

Figure 12 is a plot of the surface sensible heat flux and x–y wind vectors at 15 m above the surface for fire $a3b3/t11q15$. For the first 22 min of each fire simulation, the near-surface winds are fairly zonal, slightly perturbed just ahead of the fire front. The initial circular spot fire grows elongated in the east–west direction (i.e. becomes cigar-shaped), as illustrated in Fig. 12 (upper plot). This pattern persists for all model fires except $a3b3/t11q15$. Plots similar to Fig. 12 for experiments $a1b3/t01q15$, $a2b3/t06q15$, and $a3b3/t08q11$ show that the near-surface winds remain fairly zonal throughout the 60 min simulations, and that there are no significant differences between, or changes in, fire size, shape, intensity, and spread-rate for these fires. Figure 12 (middle plot), however, shows the beginning of a reversal of the near-surface winds in experiment $a3b3/t11q15$ at 26 min into the simulation. At approximately 30 min into the simulation, the near-surface winds ahead of fire $a3b3/t11q15$ are completely reversed, blowing back towards the fire. In the next minute the winds pick up speed, and this increase lasts for the next 6 or 7 min. These sudden changes in the wind field correspond in time with the sudden changes in *SR*, *CI*, and *GI* seen in Fig. 11. At 32 min into the simulation (Fig. 12, lower plot), the surface winds are strong and blowing west to east throughout the entire fire domain. Although the fire $a3b3/t11q15$ is decreased in perimeter, the ground fire flux reaches an intensity of 124 kW m^{-2} at 32:24 (minutes:seconds).

In order to understand why model fire $a3b3/t11q15$ exhibited such behavior, the u, v, BU, Q, and V_y fields are presented. Figures 13–19 attempt to convey the dynamic differences between each fire and what events lead to the 6 min 'blow-up' of model fire $a3b3/t11q15$. The times chosen for display are 26:00, 31:36, and 32:40 (minutes:seconds), and the model fires chosen for display are $a1b3/t01q15$,

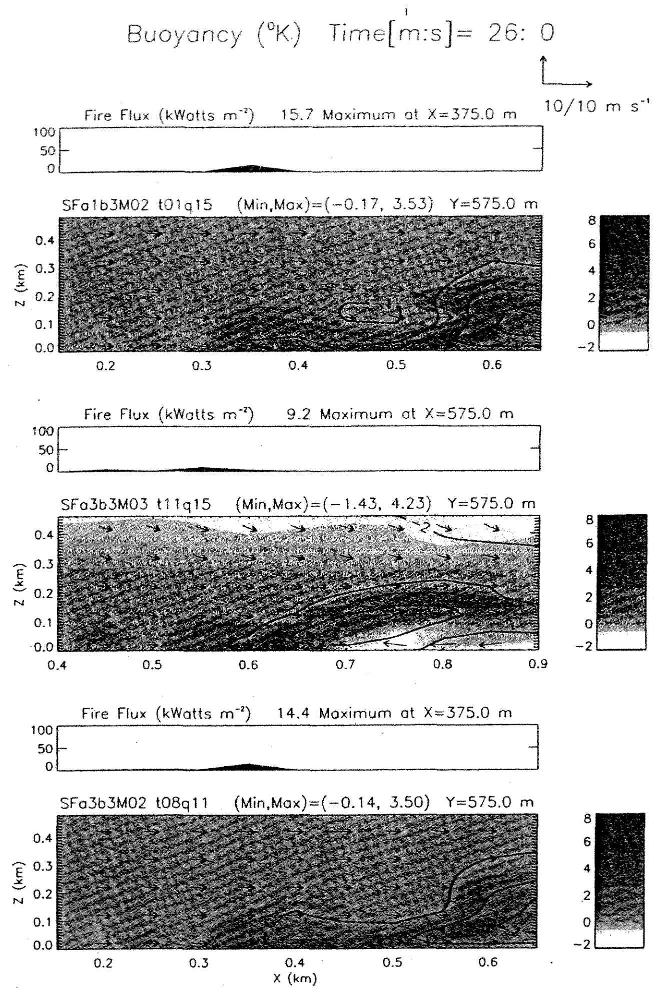

Fig. 13. x–z cross-sections of buoyancy *BU* at $y = 575.0$ m and time 26:00 (minutes:seconds) for experiments $a1b3/t01q15$, $a3b3/t11q15$, and $a3b3/t08q11$, and respective plots of fire flux (sensible heat flux). The x position of maximum fire flux values and the maximum and minimum *BU* values for each experiment are indicated. The vectors represent the winds in the x–z plane. The solid contour lines represent vertical motion in m s^{-1}.

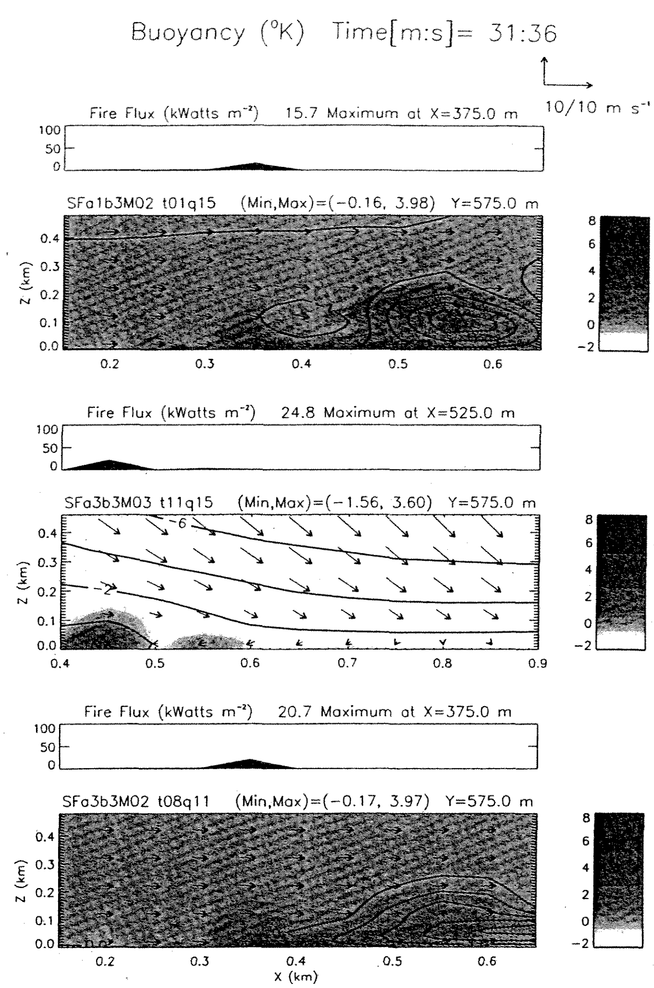

Fig. 14. Same as Fig. 13 except for time 31:36 (minutes:seconds).

$a3b3/t11q15$, and $a3b3/t08q11$. Experiment $a2b3/t06q15$ is not shown; the results indicate that the behavior of this fire was not substantively different from that of fire $a1b3/t01q15$ or fire $a3b3/t08q11$. Vertical cross-sections of BU and Q are also presented, as an examination of the fields at upper levels indicate that BU and Q were significantly changed as the fire and wind field evolved.

Figure 13 is a plot of buoyancy BU at 26:00 (minutes:seconds) into the simulations. The plots for experiments $a1b3/t01q15$ (upper) and $a3b3/t08q11$ (lower) show positive BU (dark grey shading) accompanying the burning areas and in the fire plume's upward moving air ahead of the fire front. Outside of the fire plume there is very weak compensating descent. The plot for experiment $a3b3/t11q15$ (middle) shows that, except for in the burning areas and the fire's plume, there is fairly significant descent throughout the fire domain and that buoyancy in the upper atmosphere is decreased. The fire–atmosphere circulation has evolved so that the initial BU field is changed by cooler (and drier) upper-level air moving down to the surface ahead of the plume, and then along the surface towards the fire front. Figure 13 (middle plot) shows negative BU at 0.7 to 0.9 km on the x axis ahead of the fire front and beneath the fire plume. Figure 14 is a plot of BU at 31:36 (minutes:seconds) into the simulation. Figure 14 (middle plot) shows that BU has continued to decrease until BU is negative almost throughout the entire fire domain. Figures 13 and 14 show that strong descending air from above and near-surface overturning has pushed fire $a3b3/t11q15$ westward by at least 50 m in the last 5 min (indicated by the locations of the fire flux maxima). These developments correspond to what was happening to *CI*, *GI*, and *SR* (Fig. 11) at this time. Negative BU just above the surface and ahead of the fire front has presumably eroded the strength of the vertical motion in the fire plume. Figuer 15 is a plot of BU at 32:40 (minutes:seconds) into the

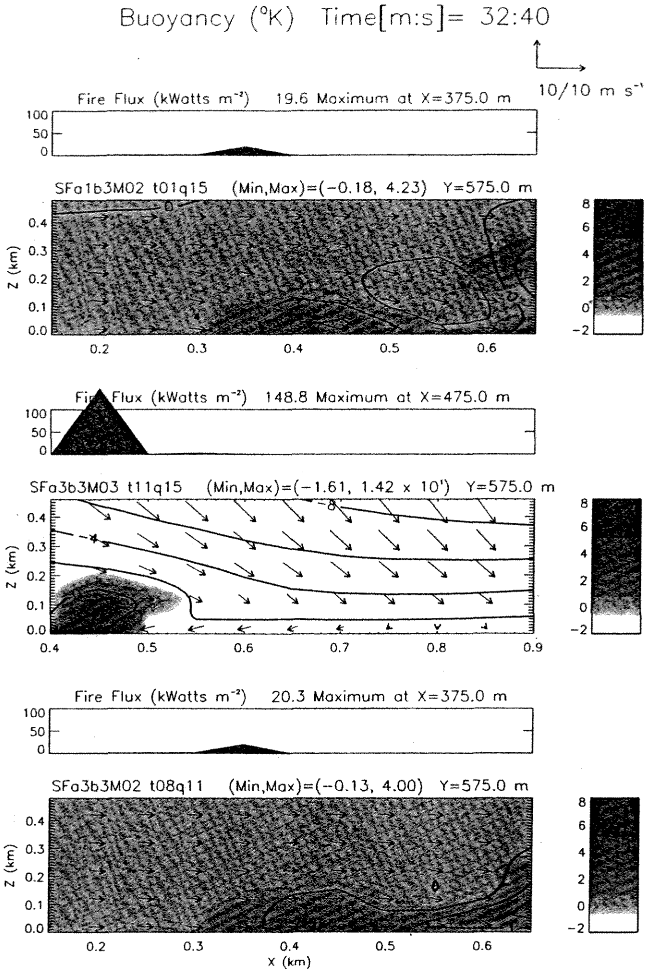

Fig. 15. Same as Figs. 13 and 14 except for time 32:40 (minutes: seconds).

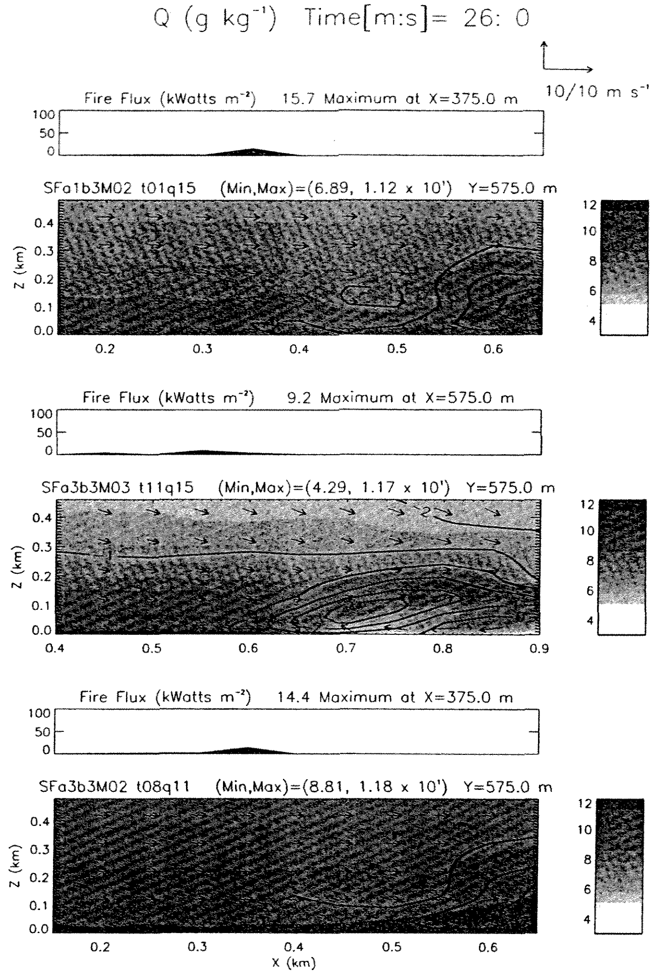

Fig. 16. Same as Fig. 13 except for water vapor mixing ratio Q.

simulation. Experiment $a3b3/t11q15$ 'blows-up' at this time. Fire flux reaches a maximum of 148.8 kW m^{-2}, upper-level descent reaches a minimum of $-8\,m\,s^{-1}$, and the fire front is pushed another 50 m west since 31:36 (minutes:seconds). Again these developments correspond to what was happening to *CI*, *GI*, and *SR* (Fig. 11) at this time. Compared to experiment $a3b3/t11q15$, experiments $a1b3/t01q15$ and $a3b3/t08q11$ behavior is not severe or erratic. The fairly benign plume behavior seen in Fig. 13 persists in Figs 14 and 15, and for the rest of the 60 min simulation time.

Figures 16, 17, and 18 are similar to Figs 13, 14, and 15 except that the field being examined is Q, the water vapor mixing ratio. Figure 16 shows that the Q fields for experiments $a1b3/t01q15$, $a3b3/t08q11$, and $a3b3/t11q15$ all have higher humidity at the surface, diminishing with height. Experiments $a1b3/t01q15$ (upper plot) and $a3b3/t08q11$ (lower plot) show higher humidity (dark grey shading) accompanying the fire plume. Experiment $a3b3/t11q15$ (middle plot) shows that the atmosphere at upper levels is already much drier (e.g. minimum Q of 4.29 g kg^{-1}) than the initial ambient humidity field. The strong descent, wind reversal, and near-surface overturning out ahead of the fire described previously are responsible for bringing down and circulating much drier air (light grey shading) into the fire plume. Figure 16 (middle plot) shows lower humidity in the air moving along the surface towards the fire front, stopping just ahead of the fire front. Low Q values are seen at 0.7–0.9 km on the x axis ahead of the fire front and beneath the fire plume. Figure 17 (middle plot) shows that Q has continued to decrease until very dry air (i.e. minimum Q of 3.53 g kg^{-1}) exists almost throughout the entire fire domain. Figures 16 and 17 show that strong descending air from above and near-surface overturning has pushed fire $a3b3/t11q15$ and accompanying humidity westward. Low humidity just above the surface and ahead of the fire front has presumably eroded the buoyancy of the air ahead of the fire front. Plots in Fig. 18 look almost identical to those in Fig. 15 except that Q, not BU, is being presented. In experiment $a3b3/t11q15$, humidity and buoyancy are weak throughout most of the fire domain, and larger values (i.e. Q maximum 7.64 g kg^{-1}

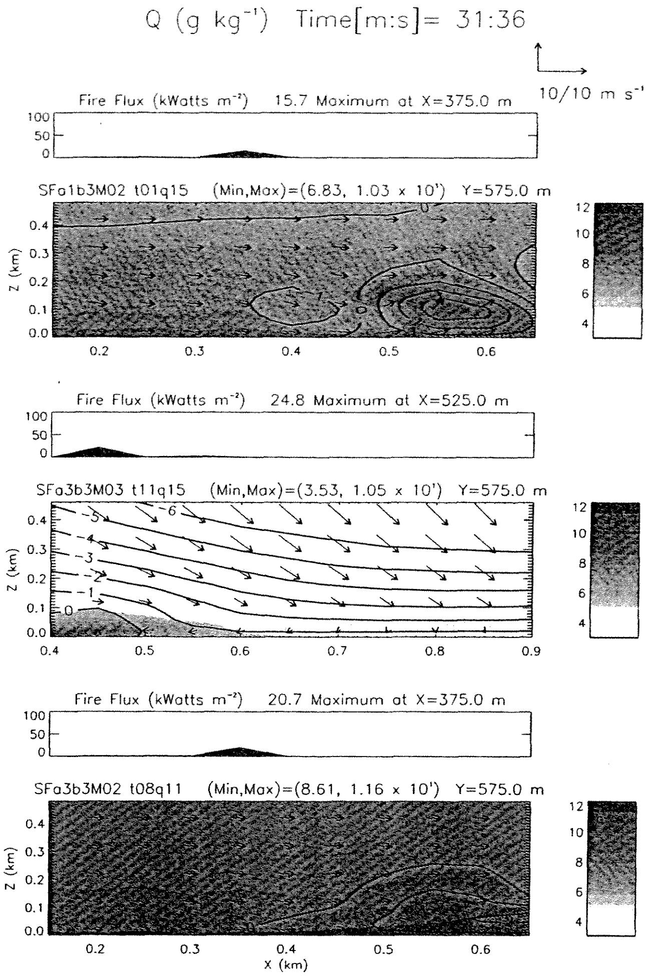

Fig. 17. Same as Fig. 14 except for water vapor mixing ratio Q.

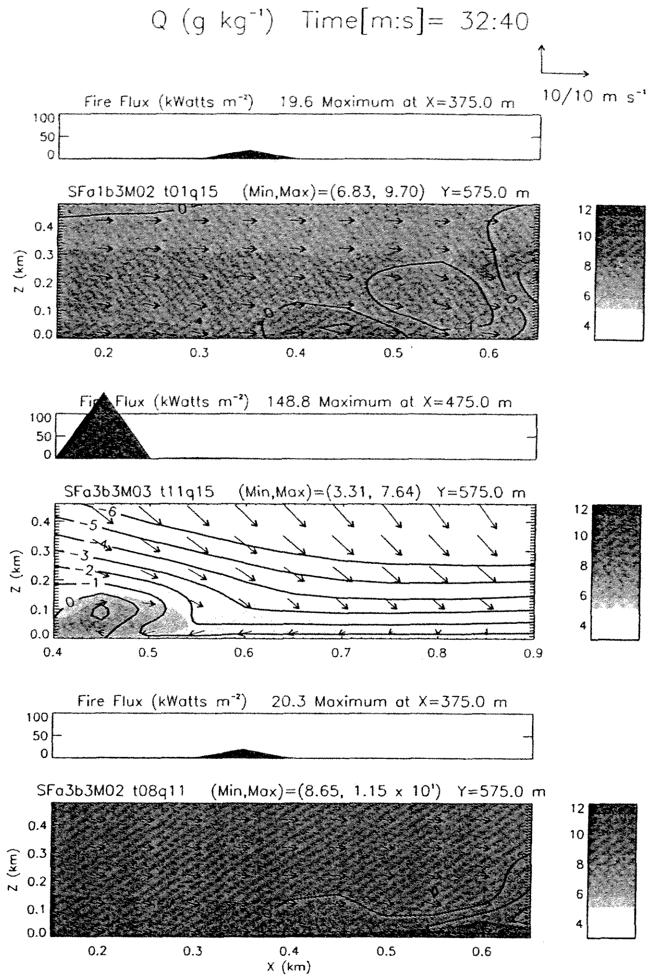

Fig. 18. Same as Fig. 15 except for water vapor mixing ratio Q.

and BU maximum 14.2°K) are confined to the first 100 m above the fire. Again compared to experiment $a3b3/t11q15$, experiments $a1b3/t01q15$ and $a3b3/t08q11$ behavior is not severe or erratic and does not lead to substantive changes in the Q field. In particular, very little change is seen in Q in experiment $a3b3/t08q11$. The fairly undisturbed Q fields seen in Fig. 16 (upper and lower plots) persist in Figs 17 and 18, and for the rest of the 60 min simulation time.

Figure 19 shows V_y, the y vorticity field, at approximately 50 m above ground level, and 26:48 (minutes:seconds) into the simulations. It was at this time in the simulations that the largest positive V_y values developed. The large area of significant and positive V_y (dark grey shading) in Fig. 19 (middle plot) indicates again strong descent and overturning out ahead of the fire front in the fire–atmosphere circulation of experiment $a3b3/t11q15$. The formation of this large fire–wind whirl is another indication that model fire $a3b3/t11q15$ developed severe and erratic fire behavior. In contrast, V_y is weakly negative out ahead of the fire front in experiments $a1b3/t01q15$ (upper plot) and $a3b3/t08q11$ (lower plot).

(9) Conclusions

The purpose of the study is to determine the relative importance of near-surface atmospheric moisture and stability to wildfire growth and evolution in a systematic and objective way. Four coupled wildfire–atmosphere model simulations are used to examine the sensitivity of wildfire behavior to lower–level environmental atmospheric stability and moisture. The sensitivity of each experimental fire to changes in these initial conditions is measured by the Taylor diagram, which is used to statistically quantify the differences between near-surface fields for each model fire. With the Taylor diagram it is possible to determine how much of the difference between model fields is due to a difference in phase and how much is due to a difference in the amplitude of the variations. The statistical differences between the four model wildfires do demonstrate the relative sensitivity during the first hour of fire simulation of dynamical and thermodynamical fields to initial conditions. The Taylor statistics show that one model fire developed severe fire behavior during this time, and the other three did not. The one model fire to respond strongly

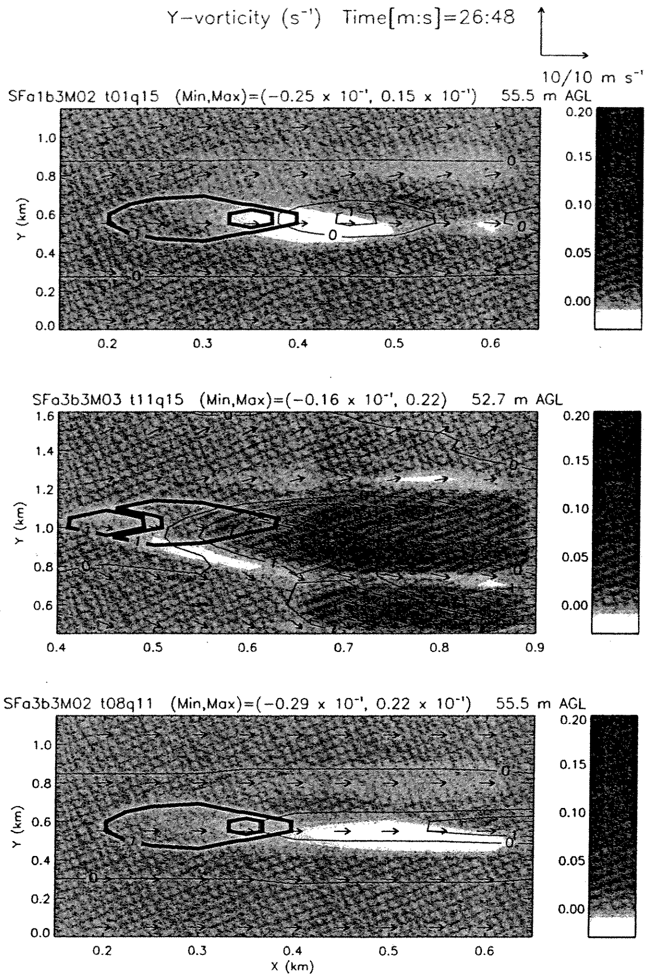

Fig. 19. x–y cross-section of V_y, the y vorticity component, at a height of approximately 50 m above ground level and time 26:48 (minutes:seconds) for experiments $a1b3/t01q15$ (reference), $a3b3/t11q15$, and $a3b3/t08q11$. The vectors represent winds in the x–y plane. The heavy solid contour lines represent sensible heat flux in $\mathrm{kW\,m^{-2}}$. The thin solid contour lines represent vertical motion in $\mathrm{m\ s^{-1}}$. The maximum and minimum V_y values for each experiment are indicated.

to the ambient initial conditions was rated as a Haines Index 6 and had the greatest lower-level atmosphere instability and dryness. Based on the Taylor statistics, several fields were chosen for further examination to try to identify the events responsible for the one case of extreme fire behavior.

The results suggest that, when the initial near-surface atmosphere is dry enough and unstable enough, a model fire can develop strong and large wildfire–atmosphere circulations that can greatly affect the evolution of the model fire and that can dramatically change atmospheric conditions throughout the model domain. Sections (6) and (7) show that nearly all near-surface fields in the model fire that did develop severe fire behavior within the first hour of simulation were changed significantly compared to the respective fields in the other fires. Section 8 shows clearly that the fire–atmosphere circulation that evolved was not confined to the local area in and around the fire, but affected the entire fire model domain. The strong descent above the fire, and wind reversal and near-surface overturning out ahead of the fire were responsible for bringing down and circulating much drier and less buoyant air into the fire plume. The results suggest that the wildfire–atmosphere circulation was responsible for eroding the buoyancy and vertical motion of the air ahead of the fire front. The near-surface overturning pushed the fire westward by at least 100 m in 4:40 (minutes:seconds), and these developments lead to an acceleration in the fire-spread rate, accompanied by a dramatic increase in heat flux from the ground fuel, and then canopy ignition and crowning. Dramatic, sudden, and simultaneous increases in fire spread rate, intensity, wind speed, and circulation and vorticity make a notable difference to someone on the ground fighting a fire, and it is worth understanding what kind and range of environmental conditions can initiate these model changes.

Results from these four numerical simulations are not conclusive. The output from a numerically simulated wildfire depends on the numerical model, fire behavior model, and fire spread-rate formula used. Model grid spacing greatly influences the results and, as discussed in Section (4), certain features characteristic of fire severity, like the development of fire-scale vortices, are not well resolved with a model grid interval of 50 m. If a grid interval of 10 or 20 m was used, it is likely that the model results would show even more significant differences between the wind and vorticity fields for each of the experimental fires. Yet, despite the grid interval of 50 m, the coupled fire–atmosphere model was able to simulate large fire whirls in the fire–atmosphere circulation when the initial atmospheric conditions were appropriate.

This is the first study to apply the Taylor diagram to analyse the differences between model variables from different numerical wildfire simulations. Useful Taylor statistics of several more fields (i.e. pressure perturbations, wind speeds, vertical wind shears, divergence in the wind fields) were determined, but not presented. Here the Taylor diagram was used to examine the surface properties of a relatively small number of fields for four numerical simulations. Future wildfire studies that need to illustrate the relative differences between any number of model variables or different observational data sets, or between the results of one coupled-atmosphere numerical prediction model and another, or to test of the effect of model changes, may find the Taylor diagram useful.

The study shows that coupled wildfire–atmosphere modeling produces results that agree qualitatively with what is observed in the field. Even though the results of this numerical modeling study are not quantitative, they are well validated by what the fire management community already knows from experience, and that is that a Haines Index greater than 5 is an indicator of high-risk fire potential. The analyses clearly indicate that low-level atmospheric stability and moisture are important for high-risk fire development when the ambient wind speeds are constant and low and there is no topography, but that there is a range of atmospheric stability and moisture conditions that is crucial to the development of severe or erratic fire behavior, and that this range is within the atmospheric conditions represented by a Haines Index 6. The results suggest that, for fires rated as a Haines Index 5 or lower, ambient atmospheric instability is not important for severe fire risk within the first hour of fire simulation, even when the atmosphere is dry. The results also suggest that, for fires rated as a Haines Index 6, ambient atmospheric stability and moisture are important factors for severe fire risk only when near-surface humidity is low enough and instability high enough.

The results have important consequences for the Haines Index. The fire management community needs accurate predictors of fire severity, especially ones that focus on the high-risk range of fire behavior. This study is a first step in the process of developing a fire–weather index that predicts actual severe or erratic fire behavior. Here only a few coupled wildfire–atmosphere simulations that cover a large range of environmental conditions are presented. The reasons for this approach were practical (limited computer capacity and disk storage), and that this study was meant as a pilot study only. A future study will be therefore to perform many coupled wildfire–atmosphere simulations, using finer grid intervals, and over a small range of environmental conditions. We aim to examine the types and relative magnitudes of severe or erratic fire behavior that fall into the range of atmospheric stability and humidity conditions that apply to a Haines Index 6. The information gained could and should be used to understood and refine or redefine the Haines Index so that it become a predictor of actual severe fire behavior.

Acknowledgements

I thank Mike Wotton, Research Officer, Fire Management Research, Canadian Forest Service, for his assistance with the Boreal forest fuel model in this study (Section 4). I am also indebted to Dr Terry Clark and Dr Janice Coen of the National Center for Atmospheric Research, Mesoscale and Microscale Meteorology Division, for providing a workstation version of the coupled wildfire–atmosphere model and fire tracing parameterization (Section 3). I also thank Dr Karl E. Taylor, Program for Climate Model Diagnosis and Intercomparison, Livermore, for supplying me with the code that helped prepare the Taylor figures (Sections 5 and 6). Reviews of the manuscript by Dr Brian Potter, Research Meteorologist, USDA Forest Service, and two anonymous reviewers are appreciated. This study was conducted while the author was a Visiting Associate Professor in the Department of Meteorology, 135 S 1460 E, University of Utah, Salt Lake City, Utah 84112-0110, USA.

References

Brotak EA, Reifsnyder WE (1977) Predicting major wildland fire occurrence. USDA Forest Service, *Fire Management Notes* **38**(2), 5–8.

Brotak EA (1993) Low-level weather conditions preceding major wildfires. USDA Forest Service, *Fire Management Notes* **53–54**, 23–26.

Clark TL (1977) A small scale numerical model using a terrain following coordinate transformation. *Journal of Computational Physics* **24**, 186–215.

Clark TL (1979) Numerical simulations with a three-dimensional cloud model: lateral boundary condition experiments and multi-cellular severe storm simulations. *Journal of the Atmospheric Sciences* **36**, 2191–2215.

Clark TL, Farley RD (1984) Severe downslope windstorm calculations in two and three spatial dimensions using anelastic interactive grid nesting: a possible mechanism for gustiness. *Journal of the Atmospheric Sciences* **41**, 329–350.

Clark TL, Hall WD (1991) Multi-domain simulations of the time dependent Navier Stokes equation: benchmark error analyses of nesting procedures. *Journal of Computational Physics* **92**, 456–481.

Clark TL, Hall WD (1995) On the design of smooth, conservative vertical grids for interactive grid nesting with vertical stretching. *Journal of Applied Meteorology* **35**, 1040–1046.

Clark TL, Jenkins MA, Coen J, Packham D (1996*a*) A coupled atmospheric–fire model: convective feedback on fire line dynamics. *Journal of Applied Meteorology* **35**, 875–901.

Clark TL, Jenkins MA, Coen J, Packham D (1996*b*) A coupled atmospheric-fire model: role of the convective Froude number and dynamic fingering at the fire line. *International Journal of Wildland Fire* **6**(4), 177–190.

Coen JL, Clark TL (2000) Coupled atmosphere–fire model dynamics of a fire line crossing a hill. Preprints of Third Symposium on Fire and Forest Meteorology, American Meteorological Society, 80th Annual Meeting, Los Angeles, CA. pp. 7–10.

García Diez EL, Rivas Soriano L, De Pablo F, García Diez A (1994) An objective model for the daily outbreak of forest firest based on meteorological conditions. *Journal of Applied Meteorology* **33**, 519–526.

García Diez EL, Rivas Soriano L, De Pablo F, García Diez A (1999) Prediction of the daily number of forest fires. *International Journal of Wildland Fire* **9**(3), 207–211.

Haines DA (1988) A lower atmospheric severity index for wildfires. *National Weather Digest* **13**, 23–27.

Hirsch KG (1996) Canadian forest fire behavior prediction (FBP) system: user's guide. Special Report 7. Canadian Forest Service, Northwest Region, Northern Foresty Centre. 122 pp.

Jenkins MA, Clark TL, Coen J (2001) 'Coupling atmospheric and fire models. Forest fire behavior and ecological effects.' (Eds EA Johnson and K Miyanishi) pp. 257–301. (Academic Press)

Jones KM, Maxwell C (1998) A seasonal Haines Index climatology for New Mexico and the significance of its diurnal variations in the elevated Southwest. Proceedings, Second Conference on Fire and Forest Meteorology, 1998, Phoenix, AZ. American Meteorological Society, pp. 127–130.

Potter BE (1996) Atmospheric properties associated with large wildfires. *International Journal of Wildland Fire* **6**(2), 71–76.

Reges II HW, Alden S (1998) Use of the Haines Index to evaluate large fire potential for interior Alaska. Proceedings Second Conference on Fire and Forest Meteorology, 1998, Phoenix, AZ. American Meteorological Society, p. 131.

Smolarkiewicz PK (1983) A simple positive definite advection scheme with small implicit diffusion. *Monthly Weather Review* **111**, 479–486.

Smolarkiewicz PK (1984) A fully multidimensional positive definite advection transport algorithm with small implicit diffusion. *Journal of Computational Physics* **54**, 325–362.

Taylor KE (2001) Summarizing multiple aspects of model performance in a single diagram. *Journal of Geophysical Research* **106**, 7183–7192.

Werth J, Ochoa R (1993). The evaluation of Idaho wildfire growth using the Haines Index. *Weather and Forecasting* **8**(2), 223–234.

Werth J, Werth P (1998) Haines Index climatology for the western United States. USDA Forest Service, *Fire Management Notes* **58**(3), 8–17.